Response to review by reviewer #1

We thank the reviewer for a constructive review, allowing us to improve our manuscript. Most of the reviewer's requests have been met. Below follow our answers and comments, highlighted in blue after each of the reviewer's comments. Blue page (P) and line(L) numbers refer to the manuscript published in TCD and red numbers refers to the marked-up revised document.

***Interactive comment on* "Signature of Arctic first-year ice melt pond fraction in X-band SAR imagery" *by* A. S. Fors et al.**

Anonymous Referee #1

Received and published: 3 September 2016

The manuscript is dedicated to the melt pond fraction estimation from X band of polarimetric SAR. This sensor is not dependent on cloud cover or presence of daylight, which is an advantage over radiometers like MODIS and MERIS. Currently, melt ponds are poorly represented in the climate models, and the melt pond research is therefore an important topic which fits well into the scope of the journal. The paper is well written and the text extensively referenced. However, the manuscript still has some potential for improvement in the points listed below.

1)The study is limited to the drifting first year ice and to the X band only; in the Introduction, the authors give a very extensive literature review which reveals a massive amount of work already published regarding SAR X and C bands for melt ponds on many ice types for many locations, among which the landfast FYI and MYI. What is the motivation for this additional study for drifting ice and X band? Drifting FYI is a widespread ice type indeed, but it features a variety of subclasses which calls for a robust method. What is the advantage of X band over other SAR bands for this challenging task?

As the reviewer highlights, many studies have already been exploring melt pond fraction retrieval from SAR. However, a majority of these studies are *single polarimetric* studies, mostly reaching vague results when it comes to melt pond fraction estimation from SAR. Only a few studies have investigated the *multi polarimetric* SAR signature of melt ponds. Among these, only one study (Han et. al 2016) has explored X-band opportunities. Han et al. (2016) focuses on one single satellite scene with known melt pond fractions, the study is performed on MYI, and very important factors like SAR incidence angle, noise floor and wind speed are not discussed. Hence, we believe there is need for more studies polarimetric X-band SAR signatures of melt ponds. To make this clearer in our manuscript, the following changes have been made:

- The following paragraph was added (Introduction, P3L90, P3L93): "In summary, the main achievements on f_{MP} retrieval with SAR come from dual polarimetric C-band studies on land-fast FYI. The potential of f_{MP} retrieval with polarimetric X-band SAR has only been explored in one single study by Han et al. (2016), focusing on MYI. Hence, there is a need for more studies on the influence of f_{MP} on polarimetric X-band SAR imagery. As MYI and land-fast FYI have been the main focus in previous studies, there is also a need to expand to other sea ice types. Drifting FYI is becoming more prominent in the Arctic with the recent shift to a thinner, more seasonal, and more mobile sea ice cover (Perovich et al., 2015), and the polarimetric SAR signature of f_{MP} in drifting FYI needs more attention."
- He following sentence was added (Introduction, P3L69, P3L71-72): "… underestimation of f_{MP}. All in all, retrieval of f_{MP} from single polarimetric SAR has proven to be difficult."

TerraSAR-X offers higher resolution than Radarsat-2, which is expected to be an advantage, due to the small size of melt ponds. X-band is also offering sensitivity to smaller surface roughnesses than C-band, which will could potentially affect the polarimetric signature beneficially. In general, it is also

important to study the effect of melt pond fractions in all operational SAR frequencies, both because they can supplement each other, and because melt pond signatures will appear differently at different wavelengths. Knowledge of melt ponds polarimetric signatures is also important for classification of sea ice in X-band scenes. To highlight these points, the following changes have been introduced in the manuscript:

- The following sentence was added (Introduction, P3L93, P4L104-107): "TerraSAR-X offers very high resolution multi-polarimetric data, with a strong sensitivity to micro-scale surface roughness due to the high frequency. Both the high resolution and sensitivity to surface roughness can be advantages in f_{MP} investigations."
- The following sentence was added (Discussion, P15L478, P18L580-581): "This is also an important result, implying useful knowledge for instance in classification of summer sea ice based on X-band imagery."

2)The study is dedicated to the comparison of helicopter-borne imagery to the dual polarisation X band SAR data. Overall, 4 SAR scenes have been taken, to which the helicopter data were possibly accurately collocated. Nevertheless, the comparison data shows considerable scatter, the Spearman correlation was used instead of Pearson (could you please justify this), and the noise equivalent was subtracted. The authors are struggling to collect all the available signal which is over the noise floor and compare it to the airborne data. However, even with this cumbersome approach, the correlation coefficients of the developed empirical relationships are Rˆ2=0.15 and 0.21, which is a very weak to weak correlation for Spearman. The authors state the surface deformation as a reason for the scatter and claim the correlation "significant" and enough to give a starting point to MPF evaluation, but the reviewer fails to see how it could work. Under these circumstances, the quality of the developed method when applied to a variety of different X-SAR images of drifting ice (even with known wind speed) is very hard to estimate, even when the one smoothes out or grids the retrieved pond fractions to coarser resolutions.

This point addresses several parts of the manuscript, and the reply is divided into 8 individual bulletpoints (a)-h)) found below.

a) Spearman's correlation coefficient was used instead of Pearson's correlation coefficient as it allows for non-linear relationships, broadening the range of detectable correlations. It is also less sensitive to outliers, which can be a problem in SAR scenes due to speckle. We have now clarified this in the manuscript:

- The following sentence was extended (Method, P9L287, P12L330-332): "A negative sign indicates an inverse relationship. Spearman's correlation coefficient assumes a monotonic relationship. It is used instead of Pearson's linear correlation coefficient, to allow for non-linear correlations. It is also less sensitive to outliers than Pearson's correlation coefficient."

We would like to note that Spearman's correlation in this study was used as a simple metric to identify SAR features potentially useful for further f_{MP} reconstruction. In the latter procedure, however, an ordinary linear regression technique was used (see point d)). We consider that in the future studies when a sufficient information on the SAR f_{MP} signature for a broad range of controlling factors have been accumulated, an application of more sophisticated multivariate techniques will be required to elaborate the model(s) robust enough for operational products. This is reflected in the manuscript:

- The following sentence was added (Discussion, P12L365, P16L508-511) "These correlations are not strong enough for the results to be used directly in operational models. However, with improved methods and more satellite data added, our results imply a future potential in retrieving f_{MP} from X-band SAR."

b) "Significant" or "statistical significant" are used several times in the manuscript, referring to correlations that are significant within a 95% confidence interval. This is clearly stated in the Results-section in the version of the manuscript published in TCD (Results, P11L351, P12L375).

c) We see that working with the signal both with and without NESZ-subtraction can be confusing for the reader. We have therefor decided to use the NESZ-subtracted signal in the manuscript, and only include values without NESZ subtraction in parentheses in Table 4. This imply the following changes:

- The following sentences were rephrased (Method, P8L230, P9L270): "All scenes were converted to ground range and radiometrically calibrated to σ^0. The noise equivalent σ^0 (NESZ) was then subtracted."
- The following sentences were rephrased (Results, P11L326-334, P12L374-385): "Values significant within a 95% confidence interval are highlighted in bold, and values in parentheses show results before NESZ subtraction of the signal. In scene T3, $R_{VV/HH}$ shows the strongest correlation to f_{MP}. In addition, the mean of α_1 is significantly correlated to f_{MP}. None of the other investigated SAR features are significantly correlated to f_{MP} in scene T3. In scene T4, the mean values of σ^0_{HH}, σ^0_{VV} and $R_{VV/HH}$ are significantly correlated to f_{MP}, the strongest correlation is found for, σ^0_{VV}. Some of the standard deviation values are also correlated to f_{MP}. Without NESZ subtraction in the calibration, however, almost all features are correlated to f_{MP}. The large difference before and after NESZ subtraction indicates that the signal is close to, or reaching the noise floor."
- The following sentence was rewritten (Discussion, P15L477, P18L579-581): In addition to $R_{VV/HH}$, five other dual-polarimetric SAR features were included in our study, after NESZ subtraction most of these showed no statistical significant relationship to f_{MP} in our data set.
- The figure caption of Table 5 was updated: "Spearman's correlation coefficient (*r*) between f_{MP} retrieved from the helicopter images at the investigated floe, and mean and standard deviation of the polarimetric SAR features from the corresponding area in T3 and T4. Bold indicate significant values within a 95 % confidence interval, and values in parentheses are retrieved before NESZ subtraction in the calibration process."
- Figures and Table 6 were updated, now presenting results after NESZ subtraction.

d) The correlation coefficients of Rˆ2=0.15 and 0.21 represent the least square regression fits of Eqs. 16 and 17 and Figs. 4 and 7, and are presented in addition to Spearman's correlation coefficient (corresponding values of -0.53 an 0.45). To clarify this in the manuscript, the regression fit correlations are renamed R_{fit}^2 (changed in Results, P12L362, P13L398, P13L421, P15L477), while Spearman's correlation coefficient is kept as *r*. For clarification, the following change was introduced:

- The following sentence was changed (Abstract, P1L7, P1L7): Co-polarisation ratio was found to be the most promising SAR feature for melt pond fraction estimation at intermediate wind speeds (6.2 m/s), with a Spearman's correlation coefficient of 0.46."

e) Due to the reviewer's comments, we revised the regression fits, and managed to improve Eq. 17 by not log-transforming σ^0_{VV}, returning a new correlation coefficient of R_{fit}^2=0.26 (previously 0.15).

- Eq. 18 was changed in the text (Results, P13L397, P15L474): "$f_{MP}(\sigma^0_{VV})$=-52.83 σ^0_{VV} +1.89"
- The following sentences were updated (Results, P13L398, P15L475): "Note σ^0_{VV} is not in dB. Again, the goodness of fit of the regression is reflecting large sample variation, with R_{fit}^2=0.26 and RMSE=0.0039.
- Figures 7, 8 and 9 were updated according to the new regression fit equation.

f) We agree with the reviewer that these correlation values are weak, and not yet suitable as a basis for operational models. It is however worth noting that the operational method used for extraction of f_{MP} from MODIS has R^2_{fit} values ranging between 0.28 and 0.45, not too far from our values of 0.21 and 0.26. We also emphasize that we do not intend to develop an operational model based on a

single SAR scene. To differentiate this we have changed the wording “model” to “regression”, “regression fit”, or ‘’estimation” in the manuscript. This modification is implemented several places in the manuscript. Hence, with improved co-location (see point g) below) and more satellite data, X-band SAR can potentially be used for f_{MP} estimation. The following changes have been made in the manuscript to stress these points:

- The following sentences were added (Results, P12L363, P13L422): “This implies a weak correlation, corresponding well to Spearman’s correlation of 0.45.”
- The following sentence was added (Discussion, P13L417, P16L506-512): “The results of this study show that f_{MP} influences the signature of several X-band polarimetric features. The strongest correlations were found for $R_{VV/HH}$ and σ^0_{VV}, where linear regression fits gave R^2_{fit} values of 0.21 and 0.26, respectively. These correlations are not strong enough for the results to be used directly in operational models. However, with improved methods and more satellite data added, our results imply a future potential in retrieving f_{MP} from X-band SAR. For comparison, the method developed for retrieval of f_{MP} from MODIS has R^2_{fit} values ranging from 0.28 to 0.45 (Rösel et al. 2012).”
- The following paragraph was rephrased (Results, P11L247-351, P13L398-403): “The melt ponds affect the polarimetric signatures in scene T3 and T4 differently (Table 4 and Fig. 4 and 5), mainly due to different wind conditions, but also due to different incidence angles and noise floors. In the following, we look closer into the feature displaying the strongest correlation to f_{MP} in each of the scenes, $R_{VV/HH}$ in T3 and σ^0_{VV} in T4.”
- The following sentence was rephrased (Results, P12L360, P15L471-474): “As for the intermediate wind case, a robust least square linear fit was applied to the data to describe the relationship between σ^0_{VV} and $f_{MP:}$”

g) From the reviewers comment, we find that the large scatter observed in the scatter plots, reflected in weak correlations values should be discussed in more detail in the manuscript. Deformation (and volume scattering in the sea ice) may contribute to the low correlation values, but another source is probably equally important. Substantial efforts were made in co-locating the helicopter photos and the floe’s position. As stated in the Method-section we estimate a possible areal offset between the helicopter images and the compared corresponding SAR pixels of up to 27%. Even a small positional offset of a few percentages would introduce random noise in the regression, lowering the correlation values. Viewed against this background, we find it acceptable to explore the effect of the regression fit on the floe and the full scenes in the data set, even if the R_{fit}^2 values are low. The following changes have been implemented in the manuscript:

- The following sentence was added (Results, P12L363, P13L423-425): “However, the co-location between the helicopter images and the sea ice floe contain some uncertainty (a maximum areal offset of 27%) possibly introducing a random error to the regression, resulting in an artificially low R_{fit}^2.”
- The following paragraph was added (Discussion P15L490, P18L605-614): “The correlations found in our study are not very strong. The weak to moderate correlations might suggest a limited sensitivity to f_{MP} in X-band SAR imagery, but they could also reflect limitations in the data set. The co-location between the helicopter images and the SAR imagery is estimated to have a possible offset of at most 27% potentially introducing a large random error into our investigation, lowering the correlation values. A larger degree of smoothing than the area covered by the helicopter images allows for might also be needed to improve the results. The absolute radiometric accuracy of TSX scenes could also influence the results of our study, but this influence is expected to be very small compared to other uncertainties. All the above-mentioned issues should be addressed in future studies.”
- The following sentence was rewritten (Conclusion, P16L515, P19L640-645): “Challenges in co-location of airborne observations and SAR imagery limited coordinated use of existing

data in our study and introduced uncertainties in our results, possibly causing artificially low correlation values."

h) We agree that the quality of the method when applied to the full satellite scenes can be hard to evaluate. To improve this, we have included the figures suggested in the reviewers point 3). We have also moderated the way we present and discuss our results in the Abstract, Discussion and Conclusion sections. Hence, the following changes are introduced:

- The following sentence was moderated (Abstract, P1L18, P1L20) "Despite this, our findings suggest new possibilities in melt pond fraction estimation from SAR, opening for expanded monitoring of melt ponds during melt season."
- The following paragraph was moderated (Discussion, P13L417-419, P16L506-607): "The results of this study show that f_{MP} influences the signature of several X-band polarimetric features."
- The following sentence was moderated (Discussion, P14L435, P16L532-534): "In our study we found a significant correlation between $R_{VV/HH}$ and f_{MP} at an incidence angle of 29° (T3), demonstrating that f_{MP} has an impact on polarimetric X-band SAR signatures also at lower incidence angles."
- The following sentence was added (Discussion, P14L444, P17L542-543): "However, the different acquisition geometry observed in Fig. 1 could also play a role."
- The following sentence was rewritten (Discussion, P15L468, 17L568-569):"A larger window size reduces the amount of speckle in the SAR scenes, which possibly explains the improvement."
- The following sentence was rewritten (Discussion, P15L475, P17L574-576)"The large sample variability observed in Fig.4 might therefore be negligible, as long as the $R_{VV/HH}$-based regression fit produces a good estimate of the mean f_{MP} for a larger area."
- The following sentence was moderated (Conclusion, P15L495, P19L618-620): "In this study we demonstrate statistically significant relations between f_{MP} and several polarimetric SAR features on drifting FYI in X-band, based on helicopter-borne images of the sea ice surface combined with four dual polarimetric SAR scenes."
- The following sentences were moderated (Conclusion, P16L497, P19L621-625): "The study reveals a prospective potential for f_{MP} estimation from X-band SAR, but also stresses the importance of including wind speed and incidence angle in a future robust f_{MP} retrieval algorithm. Such an algorithm could supplement optical methods, and be used as a tool in climate applications, both as input in climate models and in studies of melt pond evolution mechanisms."
- The following paragraph was moderated (Conclusion, P16L505-512, P19L627-636): "The theoretical range of suitable wind speeds (<5 m/s) and sea ice surface roughnesses (s_{RMS}<1.4 mm) for f_{MP} extraction based on $R_{VV/HH}$ are slightly more limited in X-band than in C-band but our results show that f_{MP} also influences the X-band SAR signature when these criteria are partly exceeded. The high noise floor of TerraSAR-X also restricted use of scenes with incidence angles above 40°, while an incidence angle of 29° gave better results. At very low wind speeds (0.6 m/s), the backscatter signal from the melt ponds became too low for f_{MP} retrieval based on polarimetric features. In that case, σ^0_{VV} was found suitable for f_{MP} estimation. In the future, use of X-band scenes can possibly increase the total amount of SAR data accessible for f_{MP} retrieval, despite their limitations compared to C-band scenes."
- The following sentence was added (Conclusion, P16L525, P20L651-653): "For development of a robust operational method, future studies should aim to include a larger number of satellite scenes acquired during various sea ice conditions, melt pond evolution stages, wind speeds and incidence angles."

a) The authors compare MPF distributions from airborne and retrieved from SAR data. To evaluate the quality of the results even better, it would be good to show also the spatial situation: the MPF retrieved from SAR plotted on a lat-lon map and the airborne reference data overplotted on the same map using same colorscale. Upon checking spatial features or spatial uniformity, the reader can make sure that the retrieved MPFs are not random numbers, but really correspond to the field situation.

We appreciate the suggestion of a spatial plot. We have now included spatial MPF figures in the manuscript. The following text and Figures are introduced to the manuscript:

- The following paragraph was added (Results, P12L382, P13L445-455): "Zooming in to the southern part of the area covered by the helicopter survey on the floe in T3, Fig. 6 *(new)* displays f_{MP} estimated from Eq. 17 with the observed f_{MP} from the helicopter images overlaid. Two different pixels smoothing windows are shown (21 x21 and 51 x 51). Note that the center pixel underlying each helicopter image frame would give the most representative value for comparison to the observed f_{MP}, as pixels closer to the frame contain a larger amount of information from outside the frame. The middle panel displays the mean estimated f_{MP} value for each frame together with the observed f_{MP} values along the track. The maps confirm some overlap between the estimated and observed f_{MP}, but also illustrates that there is room for improvement. The estimation with a 51 x51 pixel smoothing window appears less variegated than the 21 x 21 estimation, and the range of the estimated f_{MP} values also corresponds better to those observed from the helicopter images in the 51 x51 estimation."
- The following paragraph was added (Results, P13L410, P15L488-497): "Figure 10 *(new)* shows f_{MP} estimated from Eq. 18 with the observed f_{MP} from the helicopter images overlaid for two different pixels smoothing windows (21 x 21 and 51 x 51). Note that the center pixel underlying each helicopter image frame would give the most representative value for comparison to the observed f_{MP}. To illustrate this, the middle panel shows the mean estimated f_{MP} value for each frame together with the observed f_{MP} values along the track. In general, a good overlap between the estimated and observed f_{MP} can be seen, even though some scatter exists. As in Fig. 6 the estimation with a 51 x 51 pixel smoothing window appears less variegated than the 21 x 21 estimation, and the range of the estimated f_{MP} values also corresponds better to those observed from the helicopter images in the 51 x 51 estimation than to those in the 21 x 21 estimation."

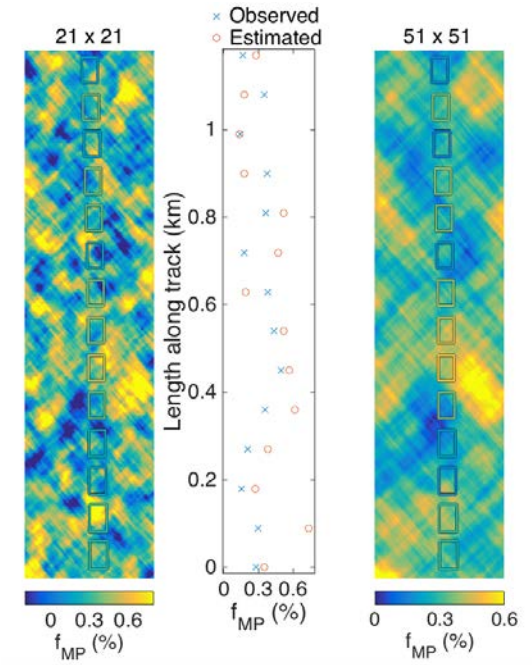

Figure caption: "Figure 6. Melt pond fraction (f_{MP}) estimated from $R_{VV/HH}$, with the observed f_{MP} from the helicopter images overlaid as colored frames. The area displayed is outlined with a frame in Fig. 5. The estimation is performed with 21 x21 (left) and 51 x51 (right) pixels windows. Note that the center pixel underlying each helicopter image frame would give the most representative value for comparison to the observed f_{MP}, as pixels closer to the frame contain a larger amount of information from outside the frame. The middle panel displays the mean estimated f_{MP} value for each frame together with the observed value."

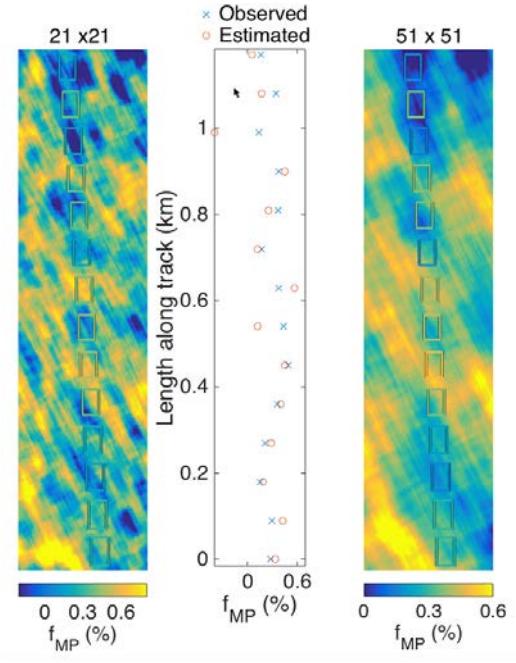

Figure caption: "Figure 10. Melt pond fraction (f_{MP}) estimated from σ_{VV}, with the observed f_{MP} from the helicopter images overlaid as colored frames. The area displayed is outlined with a frame in Fig. 8. The estimation is performed with 21x21 (left) and 51 x 51 (right) pixels windows. Note that the center pixel underlying each helicopter image frame would give the most representative value for

comparison to the observed f_{MP} as pixels closer to the frame contain a larger amount of information from outside the frame. The middle panel displays the mean estimated f_{MP} value for each frame together with the observed value."

The authors come to the conclusion that the dual polarimetric SAR data in X band can be used for melt pond estimate given the appropriate wind speed, incidence angle, surface deformation ranges and also upon extensive smoothing or even taking the mean value over the whole scene.

The impact and importance of such a product is not sufficient for advancing our under-standing on melt pond processes and can only serve as complementary data for other studies. Currently, the manuscript serves more as a fundamental study on the SAR features in X band and more displays limitations than advantages of the data.

We agree that the manuscript can be seen as a fundamental study on polarimetric SAR features in X-band, and their relation to melt pond fraction, testing a potential method for melt pond fraction retrieval. Producing an operational product for estimation of melt pond fraction from (X-band) SAR will take more than one single study. To advance in this process, it is very important to focus on possible limitations like surface roughness ranges and wind speed, and optimum SAR parameters like incidence angle and smoothing window size (stated in Conclusion, P15L522-529, P19649-654). This allows for more precise and to the point studies in the future. Hence, we think our study presents important results for future development of melt pond fraction retrieval from X-band SAR.

I recommend to support the shown MPF results with possibly more SAR scenes and definitely show the spatial MPF maps to confirm the quality of the pond retrieval, or refocus the manuscript on signatures of various ice/pond types in X band without the actual MPF retrieval.

SAR-scenes with corresponding ground truth are very rare, being generally a result of coordinated campaigns, and in this data set, we are limited to the presented scenes. As detailed above, we have included the requested MPF maps (new Figs 6 and 10), allowing the reader to confirm the quality of the presented method.

Technical
- Please add the error bar of the empirical fit in Eq. (16) and (17) on the corresponding figures, this helps to estimate the quality of the MPF retrieval.

95% confidence intervals were added in Figure 4 and 7.

- please add the correlation coefficient values into the abstract and into figure captions where you present the empirical fits.

Correlation coefficient values were added into the figure captions of Figure 4 and 7, and into the abstract:

- The following sentence was rephrased (Abstract P1L10, P1L9-13): "To further investigate these relations, regression fits were made both for the intermediate (R^2_{fit} =0.21) and low (R^2_{fit} =0.26) wind case, and the fits were tested on the satellite scenes in the study."

- I suggest to merge the subsection 4.1 Sea ice conditions into the subsection 3.1 Study region. Current section 4.1 logically fits better to 3.1.

The subsections have been merged, and are now united in subsection 3.1 renamed "Study region and sea ice conditions".

Response to review by reviewer #2

We thank the reviewer for constructive criticism, allowing us to improve our manuscript. A majority of the reviewer's requests have been met. Below follow our answers and comments, highlighted in blue after each of the reviewer's comments. Blue page (P) and line (L) numbers refers to the manuscript published in TCD and red numbers refers to the marked-up revised version.

General comments

The authors have studied melt pond fraction (MPF) estimation using TerraSAR-X dual-polarization SAR imagery acquired over drift ice north of Svalbard, and presented empirical models for MPF estimation in two different wind speed conditions (low speed and intermediate speed).

In the Introduction Section authors give good overview on importance of melt ponds on the Arctic sea ice heat budget and in the Arctic climate system, and on previous studies on melt pond fraction estimation with optical and SAR imagery. The number of previous SAR studies on melt pond detection and fraction estimation is quite large, and so far a generic method for the estimation has not been presented/developed. There has been some success for the melt pond fraction (MPF) estimation over smooth landfast ice using C-band co-polarization ratio (HH and VV pol SAR images needed) or HH-pol backscattering coefficient (σ). For MPF estimation over drift ice only few studies has been conducted. At least it seems that MPF estimation over drift ice with C-band single pol imagery is not possible. Over drift ice sea ice deformation features like ice ridges and make MPF estimation in theory much more difficult than over smooth landfast ice. Other frequencies than C-band have been used only in few case studies. Likely (to my opinion) accurate MPF estimation is only possible with high resolution (<5-10 m) SAR imagery. So far time series of MPF maps over the Arctic have been produced only with optical imagery (MODIS, MERIS). These charts are limited by accuracy of automatic cloud masking and persistent cloud cover during the Arctic summer. Accurate MPF charts from SAR imagery would supplement greatly the MPF charts from optical imagery.

Section 2 discusses nicely about melt pond signatures in SAR imagery, but it could also include overview of observed MPF behavior during melt ponding season (ponding, drainage etc.), see e.g. D. G. Barber, J. J. Yackel, and J. M. Hanesiak, "Sea ice, RADARSAT-1 and arctic climate processes: A review and update," Can. J. Remote Sens., vol. 27, no. 1, pp. 51–61, 2001.

We appreciate this suggestion, and have included a brief comment on this in the manuscript.

- The following sentences were added (Melt ponds in SAR imagery, P4L113, P4L127-130): The coverage of melt ponds varies during the melt season, starting out with a high fractional cover, and reducing as the ponds drain. At the end of the melt season, the melt ponds refreeze. This evolution is mirrored by a seasonal variation in the sea ice SAR signature (Barber et. al 2001)."

Dual-polarization TerraSAR-X imagery acquired over drift ice for MPF estimation have been previously studied by Kim et al. (2013) and Han et al. (2016). Kim et al. (2013) used only one TSX image acquired in Aug 2011 over East Siberian Sea, but they have large amount of co-incident airborne very fine resolution X-band (single pol) images. Comparison MPF data was from airborne photography. Han et al. (2016) used the same datasets and also one additional TSX image acquired in July 2011 over the Chukchi Sea. Kim et al. (2013) estimated MPF with "We first delineate the ice and melt pond features using image processing software (ENVIA EX), based on the combination of multiscale segmentation and aggregation methods."; not discussed in more details, but Han et al. (2016) studied various polarimetric parameters and their textural features in MPF estimation by machine learning approaches.

The authors have used here four TSX dual-polarized StripMap images acquired during ICE2012 campaign in north of Svalbard. Comparison MPF data was from helicopter-borne optical imagery. In addition, surface roughness data was calculated from stereo camera imagery, and weather data was measured by R/V Lance at the ICE2012 campaign site. They have studied MPF estimation with different polarimetric parameters calculated from the dual-pol TSX imagery, as was done also by Han et al. (2016). The main questions now are: 1) Does this study give new scientific results/information compared to Kim et al. (2013) and Han et al. (2016)? 2) In what ways it is different to them, data and/or methods?

My answers: Study area is different (Chukchi Sea vs. Svalbard) which could have influence on the results if sea ice conditions (FYI vs. MYI) where different; authors should discuss this in the paper. Wind speed is taken into account here unlike in Kim et al. (2013) and Han et al. (2016). Wind speed has large effect on the backscattering from melt ponds (not frozen). Somewhat more SAR images have used, four here compared to two in Han et al. (2016), making the results here more reliable. The developed MPF algorithms are linear functions between MPF and one polarimetric parameter. I favor this kind of simple approach as the results can be related easily to theoretical backscattering models. Han et al. (2016) utilized machine learning approaches where relations between polarimetric parameters (and scattering theory) and an estimated parameter may not be very clear. However, I think that the paper in its current form gives quite little new information/findings compared to previous studies on the MPF estimation with SAR.

We appreciate the papers by Kim et al. (2013) and Han et al. (2016), which as our study focus on melt ponds and SAR. Kim et al. (2013) focuses on airborne SAR and barely discuss satellite imaging and is hence very different from our study. Han et al. (2016) presents a machine learning approach for melt pond fraction retrieval from X-band SAR based on two satellite SAR scenes, one that has corresponding information about actual melt pond fraction.

As the reviewer has commented on, there are several differences between the study of Han et al. (2016) and our study. Han et al. (2016) focuses on MYI, and explicit request more studies on other sea ice types in their conclusion. Our manuscript focuses on level FYI, which has different microwave signature than MYI, as commented on in Han et al. (2016). The effect of sea ice surface roughness, satellite noise floor, wind speed, and incidence angle are not discussed in Han et al. (2016), but wind speed and incidence angle are suggested to be investigated in future studies. These are important factors in understanding the melt pond signature of X-band SAR and are therefore included in our study, adding essential information. Only one scene with corresponding melt pond information was employed by Han et al. (2016. Increasing the number of scenes, as done in our manuscript, is of large importance to improve the understanding of melt ponds signature in SAR imagery.

While Han et al. (2016) focuses on combining several polarimetric signatures in machine learning algorithms for melt pond retrieval, our manuscript concentrates about the individual polarimetric features, and the influence of melt ponds on these. This could form a basis for more advanced methods later on, guiding which features to use under specific wind speed conditions and incidence angles. Melt ponds and sea ice are treated as different classes in the study of Han et al. (2016). Our study on the other hand, focuses on the signature of mixtures of melt ponds and sea ice.

When it comes to the results, different polarimetric features are found sensitive to melt pond fraction in Han et al. (2016) and our study. While co-polarisation ratio and HH intensity were the most promising features in our study, co-pol phase difference, alpha angle, and HH intensity were found to be the most important ones in Han et al (2016). This could be due to e.g. difference in wind conditions, which there is little information about in the study by Han et al. (2016).

In summary, we find that Han et. al (2016) and our study does not present much overlapping information and findings, hence our study are complementary. The sea ice types, methods and results are different, and our study includes several factors (more scenes, wind speed, incidence angle, surface roughness etc.) not considered in Han et al. (2016). To evolve in the understanding of melt ponds signatures and impact on X-band SAR, and SAR in general, a variety of studies is necessary, and we believe our study contributes with enough new insight, and is worthy of publication.

To clarify the differences in the study of Han et al. (2016) and our study for the readers of our manuscript, the following changes have been applied:

- The following sentences were rephrased (Introduction, P3L82, P3L85-91): "Han et al. (2016) combined multiple polarimetric SAR features in MPF estimation by machine learning methods, employing the co-polarisation channels of the MYI X-band SAR scene explored in Kim et al. (2013). An additional scene was also included in the study, though without melt pond information. The study showed promising results, but the authors claim that more scenes with various sea ice types and incidence angles are needed to develop a general propose MPF model. Lack of wind information is also limiting the relevance of the study."
- The following paragraph was added (Discussion, P15L490, P18L592-604): "The findings in our study deviate from the findings of Han et al. (2016) where σ^{o}_{HH}, < ρ, and, α_1 were found to be the most prominent polarimetric features in separating melt ponds, sea ice and open water in high resolution X-band SAR imagery. Differences in sea ice type, sea ice surface roughness, wind conditions, and SAR incidence angle could possibly explain why different polarimetric features are sensitive to MPF in the two studies. The methods of the two studies are also slightly different, as Han et al. (2016) classify each pixel into melt pond, sea ice or open water, while our study focuses on mixtures of melt ponds and sea ice. Exact wind information lacks in Han et al. (2016) but the wind speed is expected to be low. This could explain why σ^{o}_{HH} contributes strongly in MPF estimation, and is then in accordance to our findings. The diverging results in the two studies emphasize the need of investigating melt ponds impact on SAR imagery under different conditions and for a variety of sea ice types. It also stresses the importance of supplementary measurements of parameters like wind speed and sea ice surface roughness."

The statistical reliability of the developed empirical MPF estimation models seems quite low, r2 was at best only 0.21 and RMSE is high.

We agree that the R^2 values for the regression fits are low. For our comment on this, see point 2f) in the reply to Reviewer #1.

The value of the paper could be improved by following changes and additions:

The empirical models for the MPF estimation were developed using datasets over a large ice floe. Why were not all co-incident SAR imagery vs. airborne photography used? How results would change if they were?
As this study was performed on drifting sea ice, co-location between SAR scenes and helicopter data is very challenging. This is also commented on in the conclusion of the manuscript. Most of the airborne photos were not possible to be co-located with the satellite observations exact enough to meet our demands of a high quality study. However, for the investigated floe, we managed to do a reliable co-location, and the floe was also the only floe appearing in two of the scenes. We therefore chose to focus on this specific floe in our investigations to secure the quality of the study.

Both wind speed and SAR incidence angle have large effect on the MPF estimation. Wind speed is now taken into account by MPF models for two different wind conditions. I suggest you developed

MPF models which include incidence angle or compensate σ incidence angle variation before MPF estimation. The study should include more variable wind speed conditions, but in the current dataset these are not present

We agree that it is desirable to study the melt pond signature under as many wind speed situations as possible to make a robust melt pond estimation. Our data set consists of four scenes, and it is therefore not possible to make such a robust model from this small dataset. However, our study highlights the importance of wind speed, and can serve as a starting point for future studies. This is already commented on in the conclusion of the manuscript.

Incidence angle correction has been introduced to the manuscript, to improve the understanding of Fig. 9. The following changes have been made in the manuscript:

- The following sentences were added (Method, P10L295, P11L340-346): " Incidence angle correction was applied to the scenes for a better comparison, employing the following equation (Kellndorfer et al., 1998)

  $$\sigma^\circ_{corr} = \sigma^\circ (\sin\theta / \sin\theta_{ref})$$

  where σ° is the original backscatter coefficient, θ is the center incidence angle of the scene to be corrected, and θ_{ref} is the reference incidence angle of scene T4. The correction was only applied in the low-wind case, as it canceled in the intermediate wind case due to the use of a co-polarisation ratio."
- The following reference was added: Kellndorfer, J., L.E., P., M.C., 715 D., and Ulaby, F. T.: Toward consistent regional-to-global-scale vegetation characterization using orbital SAR systems, IEEE Transactions on Geoscience and Remote Sensing, 36, 1396-1411, doi:10.1109/36.718844, 1998.
- The following sentence was rewritten (Results, P13L413, P15L501-502): "Incidence angle correction according to Eq. 16 is applied to the figure, accounting for σ°_{VV} decrease with incidence angle."
- The following sentence was rewritten (Discussion, P14L449, P17L548-550): "The underestimation of FMP in scenes T1-T3 is likely related to higher wind speeds at the time of acquisition."

You could study effect of sea ice type in the MPF estimation, e.g. by first segmenting the SAR images to level ice and deformed ice categories (with the help aerial photography if possible). In best case we could have also sea ice type taken into account in the MPF estimation. You have also surface roughness data which could be utilized here.

We agree that the effect of surface roughness could be better presented in the manuscript. We have now introduced two classes of sea ice in the scatter plots (Fig. 4 and 7), representing totally level ice and partly deformed sea ice. The classification is based on visual interpretation of the helicopter images. The following changes have been introduced in the text in relation with the classification:

- The following sentences were added (Results, P11L355, P13L408-411): Grey dots correspond to areas with some degree of sea ice deformation, while blue dots correspond to areas with completely level ice. Deformation information is extracted from visual inspection of the helicopter images."
- The following sentence was rewritten (Results, P12L358, P13L414-416): "A majority of the lowest $R_{VV/HH}$ values are appearing in partly deformed areas. Areas with some degree of deformation also represent the lowest f_{MP}."
- The following sentence was added (Results, P13L395, P15L470-471): "Grey dots correspond to partly deformed areas, while blue dots represent level ice."

Show MPF maps from some SAR images and discuss spatial variation present, does it make sense? You have four SAR images, how does estimated MPF behave temporally? Now Table 5 shows MPF averages over the full scenes, but these are not much discussed in the text, and temporal variation does not seem right (36.2->45.7->31.2->53.3).

Spatial MPF maps have been introduced to the manuscript. See comments to point 3) in the reply to Reviewer#1.

During the campaign, the MPF was stable with a mean of 33.2%. The variation seen in Table 5 is due to differences in wind speed conditions and incidence angle. This is thoroughly commented on and discussed in the last paragraph of section 4.1 (New 3.1) and in the third paragraph in section 5 (Discussion).

Can you compare your estimates with those from optical imagery? See http://icdc.zmaw.de/1/daten/cryosphere/arctic-meltponds.html

The suggested data set lasts until 2011, and can therefore not be used in our study. We agree that it would be interesting to compare our data to optical data, and investigated this opportunity early in the manuscript process. However, there were cloudy conditions during the campaign, and optical data were therefore not accessible. This underlines the advantage of a possible melt pond fraction estimation from SAR.

The study would benefit greatly from a larger SAR dataset. Are there any co-incident TSX vs. in-situ / airborne data from NICE2015 campaign you could use? You really need more wind speed conditions for the MPF estimation development. Even including more TSX images without corresponding comparison data is possible, you could study spatial and temporal trends. In addition, any fine resolution C-band images available? Comparison between C- and X-band would be nice addition.

We agree that one should aim to use as many SAR scenes as possible in a study like this. But this has to be balanced by the actual access to scenes with high quality information about melt pond fraction and sea ice conditions retrieved from in situ measurements and helicopter photos. Such data sets are very rare, and it is therefore important to publish results from existing data sets, even if they as in our case have a limited number of scenes.

The N-ICE-2015 campaign was finished in mid-June 2015, before the onset of intense surface melt, and data from this campaign is therefore not appropriate for our study. C-band scenes were planned collected during the campaign, but acquisition priorities hampered collection of such scenes. We have also attended other campaigns with intention of increasing the data amount. The lack of success with these efforts emphasizes the value of the presented data set.

In general, the paper is well written and structured, and easy to read and understand. The data processing and analysis methods are scientifically sound and discussed in needed detail. I am afraid in the current form the paper gives quite few new scientific findings compared to previous studies.

We appreciate that the reviewer likes our manuscript. The novelty of this study is already discussed above. We find that our study brings in new and different findings compared to the only other existing study on the topic (Han et al. 2016), and we believe it is worthy of publication.

From Conclusions: “Future studies should aim to include a larger number of satellite scenes acquired during various sea ice conditions, melt pond evolution stages, wind speeds and incidence angles. The effect and limitations of sea ice surface roughness and dependency on filtering size and scale should also be further investigated.”

You should consider taking some of these topics to this paper!

Wind speed, incidence angle, surface roughness, and filtering size are all discussed in our manuscript. This sentence simply states that more data is needed to make a robust algorithm for melt pond fraction retrieval in X-band. To make this absolutely clear, we have rewritten the sentence:

- The following sentences were rewritten (Conclusion, P16L525, P19L651-654): "For development of a robust operational method, future studies should aim to include a larger number of satellite scenes acquired with various sea ice conditions, melt pond evolution stages, wind speeds, and incidence angles. The effect and limitations of sea ice surface roughness and dependency on filtering size and scale should also be further investigated."

Finally, Yackel and Barber (2000) speculated that MPF may be more closely related to the albedo than to melt pond fraction due to the fact that albedo results from the integration of all surface types (snow, saturated snow, melt ponds) which contribute to the measured MPF. What's the authors' view on this; would it be better to investigate the relationship between SAR data and albedo than SAR and melt pond fraction? Please, discuss this in Introduction Section.

This question might have a typing error, and we find it slightly unclear. We interpret the question to ask whether estimated melt pond fraction should be compared to albedo instead of observed melt pond fraction. Albedo refers to the average reflection of waves in the visible range of the microwave spectrum. As SAR uses microwaves to evaluate the sea ice surface, we find it more credible to utilize differences in the microwave signature between melt ponds and sea ice, or methods that employ statistical features describing fractional mixtures of surfaces.

In our study, albedo is not measured, and would have to be estimated by upscaling from melt pond fraction measurements and in situ measured albedo values of different surface types. This method would inevitably introduce additional uncertainty to the results (see f.ex. Divine et al., 2015 for estimates made for the study area), and is therefore not advisable for our data set. The relationship between albedo and polarimetric features will therefore not be discussed in detail in our manuscript.

Specific comments

1.Introduction

page 3, lines 90-92: terms 'dual polarimetric' and 'dual-polarisation' used, confusing…I think it should be 'dual-polarisation' for SAR imagery with two polarizations.

We agree in this, and have changed the term:

- The following sentence was rewritten (Introduction, P3L90-92, P4L101-103): "The objective of this study is to investigate the potential of melt pond fraction retrieval from level drifting FYI with dual-polarisation X-band satellite SAR. A data set consisting of four high resolution dual-polarisation TerraSAR-X satellite scenes…"

2. Melt ponds in SAR imagery

p. 4, l. 118: "Observed surface roughness increases with increasing frequency, making X-band more sensitive to small-scale surface roughness than C-band."
I think surface roughness is physical property of a surface, and its effect on backscattering depends on radar wavelength.

We agree that this sentence was unprecise, and have rewritten it:

- The following sentence was rewritten, (Melt ponds in SAR imagery, P4L118, P5L135-137): "X-band is more sensitive to small-scale surface roughness than C-band, as the effect of surface roughness depends on radar wavelength."

l. 124: “Six of these features are included in our study and are described in the following subsection.” In Table 4 there are eight features.
This is correct, and we have corrected the sentence:

- The following sentence was rewritten (Melt ponds in SAR imagery, P4L124, P5L142): “Eight of these features...”

3.2 Data set
Give absolute calibration accuracy and equivalent number of looks (ENL) (i.e. effect of radar fading) in TSX images. Do they have any significant effect on your data analysis results?

The absolute radiometric calibration accuracy is 0.6 dB. This parameter is an image-wide measure and includes temporal drift. Hence, it probably varies more from near-range to far-range than in a local region. As we focus on small regions in our main analysis, this accuracy will probably not play a significant role. However, for development of a future operational algorithm across many images, the calibration accuracy might be of importance. We therefore include the accuracy in our manuscript, and note that it should be further explored in future studies. The following changes were introduced in the manuscript:

- The following sentence was added (Method, P8L231, P9L272): “The absolute radiometric calibration accuracy of TSX is 0.6 dB (Airbus Defense and Space, 2013).”
- The following sentence was added (Discussion, P15L490, P18L611-614) “The absolute radiometric accuracy of TSX scenes could also influence the results of our study, but this influence is expected to be very small compared to other uncertainties.”

ENL is a far more complicated issue, and we do not see how including this would strengthen the manuscript. We are not statistically modelling the speckle distributions, and only look at the mean values after smoothing. ENL does have some bearing on the degree of variation, but this is directly evident form our observations without the complication of trying to interpret the effect of ENL. Also, radar texture, or non-Gaussianity, which is observed to be high for TSX imagery, is a far more influential factor. All simple ENL measures are Gaussian-based estimates, which do not correctly capture the texture aspect, and could lead to incorrect interpretation. Based on these reflections, we have decided not to include ENL in the manuscript.

4.1 Sea ice conditions
Was there any nighttime re-freezing on sea ice and melt pond surfaces which could have influenced backscattering signatures in T1 TSX image acquired at 06:52 UTC on 28 July?

Nighttime refreezing was not observed during the campaign, and is therefore unlikely to have influenced any of the SAR signatures. This is now clarified in the manuscript:

- The following sentences were changed/added (Method, P10L314, P8L256-257): “Air temperatures were varied little between -1 to 1.5C. Combined with the oceanic heat flux, the ice was therefore in continuous melt even at nighttime.”

4.3 Intermediate-wind case
p. 12, l. 358: “From visual inspection of the helicopter images, some of the lowest RVV/HH values origin from slightly deformed areas with a surface roughness possibly exceeding the Bragg criterion.” Please discuss how this sea ice condition leads to low RVV/HH.

We agree that this should be better described. We have therefore expanded the sentence with a possible explanation of the low values.

- The following sentence was rewritten (Results, P12L358, P13L411-414): “The partly negative values of RVV/HH imply that $\sigma^0_{HH} > \sigma^0_{HH}$. This might be a result of multiple scattering events in the sea ice volume or sea ice surface, possibly connected with sea ice deformation.”
- The following sentence was rewritten (Discussion, P14L460, P17L559-560): **“**Multiple scattering events in the sea ice surface and sea ice volume may also have contributed to the large sample variations observed in Figs. 4 and 8.

Manuscript prepared for The Cryosphere
with version 2015/04/24 7.83 Copernicus papers of the LaTeX class copernicus.cls.
Date: 25 November 2016

Signature of Arctic first-year ice melt pond fraction in X-band SAR imagery

Ane S. Fors[1], Dmitry V. Divine[2,3], Anthony P. Doulgeris[1], Angelika H. H. Renner[2,4], and Sebastian Gerland[2]

[1]Department of Physics and Technology, University of Tromsø - The Arctic University of Norway, 9037 Tromsø, Norway
[2]Norwegian Polar Institute, FRAM Centre, 9296 Tromsø, Norway
[3]Department of Mathematics and Statistics, University of Tromsø - The Arctic University of Norway, 9037 Tromsø, Norway
[4]Institute of Marine Research, 9294 Tromsø, Norway

Correspondence to: Ane Fors (ane.s.fors@uit.no)

Abstract. In this paper we investigate the potential of melt pond fraction retrieval from X-band polarimetric synthetic aperture radar (SAR) on drifting first-year sea ice. Melt pond fractions retrieved from a helicopter-borne camera system were compared to polarimetric features extracted from four dual polarimetric X-band SAR scenes, revealing significant relationships. The correlations were strongly dependent on wind speed and SAR incidence angle. Co-polarisation ratio was found to be the most promising SAR feature for melt pond fraction estimation at intermediate wind speeds (6.2 m/s), with a Spearman's correlation coefficient of 0.46. At low wind speeds (0.6 m/s), this relation disappeared due to low backscatter from the melt ponds, and backscatter VV-polarisation intensity had the strongest relationship to melt pond fraction with a correlation coefficient of -0.53. ~~From the results, an intermediate and a low-wind speed empirical model for melt pond fraction estimation were suggested and evaluated. The models~~ To further investigate these relations, regression fits were made both for the intermediate ($R^2_{fit} = 0.21$) and low ($R^2_{fit} = 0.26$) wind case, and the fits were tested on the satellite scenes in the study. The regression fits gave good estimates of mean melt pond fraction for the full satellite scenes, deviating with less than 4% from the airborne retrieved melt pond fractions in the investigated area. A smoothing window of 51×51 pixels gave the best reproduction of the width of the melt pond fraction distribution. A considerable part of the backscatter signal was below the noise floor at SAR incidence angles above $\sim 40°$, restricting the information gain from polarimetric features above this threshold. Compared to previous studies in C-band, limitations concerning wind speed and noise floor set stricter constraints on melt pond fraction retrieval in X-band. Despite this, our findings ~~demonstrate~~ suggest new possibilities in melt pond fraction estimation from SAR, opening for expanded monitoring of melt ponds during melt season. In the next step, melt pond estimation from SAR may supplement surveillance from optical satellites, providing melt pond information to climate applications during cloudy conditions.

1 Introduction

Melt ponds form from snow and ice melt water on the Arctic sea ice during spring and summer, and can cover up to $50-60\%$ of the sea ice surface (Perovich, 2002; Eicken et al., 2004; Inoue et al., 2008; Perovich et al., 2009; Polashenski et al., 2012). Their presence affects the heat budget of the sea ice by decreasing the surface albedo, which increases the solar absorption in the ice volume and the transmission of solar energy to the ocean (Eicken et al., 2004; Ehn et al., 2011; Nicolaus et al., 2012; Perovich and Polashenski, 2012). The transmission is generally larger for first-year ice (FYI) than for multiyear ice (MYI) due to FYI's lower sea ice thickness. (Light et al., 2008; Nicolaus et al., 2012; Hudson et al., 2013). FYI also often experiences higher melt pond fractions (f_{MP}) than MYI (Fetterer and Untersteiner, 1998; Nicolaus et al., 2012). The increased absorption induced by melt ponds accelerates the decay of sea ice, and the intensified warming of the ocean possibly delays the ice growth in the autumn (Flocco et al., 2012; Holland et al., 2012; Hudson et al., 2013; Schröder et al., 2014; Flocco et al., 2015). Formation and evolution of melt ponds are poorly represented in sea ice models, potentially contributing to an underestimation of the observed sea ice extent reduction in model projections (Flocco et al., 2012; Holland et al., 2012; Flocco et al., 2015). An increased number of observations of melt pond fraction (f_{MP}) for different sea ice types at regional scale is needed to improve the understanding of the role of melt ponds in the Arctic climate system. Satellite imagery offers good opportunities for such large scale monitoring of melt ponds.

Several algorithms have been developed for retrieval of melt pond fraction from optical satellites, measuring the spectral reflectance from open water, sea ice and melt ponds. The algorithms apply to different multispectral sensors; the enhanced thematic mapper plus (ETM+) on board Landsat 7 (Markus et al., 2003; Rösel and Kaleschke, 2011), moderate-resolution imaging spectroradiometer (MODIS) on board Aqua and Terra (Tschudi et al., 2008; Rösel et al., 2012; Rösel and Kaleschke, 2012), and medium resolution imaging spectrometer (MERIS) on board Envisat (Zege et al., 2015; Istomina et al., 2015). Commonly, the retrieval algorithms are vulnerable to correction for atmospheric constituents and influences of the viewing angles and the solar geometry. They also require cloud-free conditions, limiting their applicability in the Arctic due to the persistent cloud cover present during summer. Satellite microwave radiometers and scatterometers can on the other hand penetrate clouds, but their resolution is in general too coarse for automated melt pond monitoring (Comiso and Kwok, 1996; Howell et al., 2006).

Satellite synthetic aperture radar (SAR) offers independence of cloud cover, atmospheric constituents, and daylight, combined with high spatial resolution. Several studies have focused on f_{MP} retrieval from single polarisation SAR, transmitting and receiving either vertical (VV) or horizontal (HH) polarised waves. Jeffries et al. (1997) developed a model for f_{MP} retrieval over MYI floes in the Beaufort sea from ERS-1 SAR satellite images, but lack of wind consideration limit the validity of the model. Wind speed was found to be a key parameter when Yackel and Barber (2000) demonstrated a significant relation between f_{MP} and HH intensity on land-fast FYI within the Cana-

dian Arctic Archipelago using SAR satellite scenes from Radarsat-1. The relationship was strong at intermediate wind speeds, but lacking at low wind speeds. Mäkynen et al. (2014) compared f_{MP} retrieved from MODIS and from a large amount of ENVISAT ASAR satellite scenes. The study area covered both FYI and MYI north of the Fram Strait. The study concluded that f_{MP} estimation was not possible based on the investigated data set. The above-mentioned studies all focus on C-band frequency (5.4 GHz) SAR. Kern et al. (2010) investigated the use of supplementary frequencies for f_{MP} retrieval on MYI in the Arctic Ocean, and showed promising results in combining C, Ku (17.2 GHz) and X (9.6 GHz) band data from a helicopter-borne scatterometer. Estimation of f_{MP} in X-band satellite SAR was further explored by Kim et al. (2013), investigating melt ponds in a TerraSAR-X scene acquired over MYI in the Chukchi Sea. Only large melt ponds were found ~~possible to detect~~ detectable in the study, leading to an underestimation of f_{MP}. All in all, retrieval of f_{MP} from single polarimetric SAR has proven to be difficult.

Dual and quad polarimetric SAR transmit and receive both vertical and horizontal waves, resulting in four possible channel combinations (HH, HV, VH and VV), and give information about the polarisation properties of the backscatter in addition to single channel intensity variations. The channels can be combined into polarimetric SAR features, e.g. channel ratios, reducing the dependency of sensor geometry. Based on C-band scatterometer measurements, Scharien et al. (2012) suggested co-polarisation ratio ($R_{VV/HH}$) to give an unambiguous estimation of f_{MP} at large incidence angles for land-fast FYI in the Canadian Arctic Archipelago and the Beaufort Sea. The topic was further investigated (Scharien et al., 2014b), and expanded to Radarsat-2 satellite scenes in Scharien et al. (2014a), demonstrating a strong potential of f_{MP} estimation from C-band dual polarimetric spaceborne SAR. Both studies were performed in the central Canadian Arctic Archipelago. The findings were partly confirmed by Fors et al. (2015), who also suggest a relationship between f_{MP} and the statistical SAR feature relative kurtosis (RK) utilizing Radarsat-2 on iceberg-fast FYI and MYI in the Fram Strait. Han et al. (2016) combined multiple polarimetric SAR features ~~for~~ in f_{MP} estimation by machine learning methods, employing the co-polarisation channels of the MYI X-band SAR scene explored in Kim et al. (2013). An additional scene was also included in the study, though without melt pond information. The study showed promising results, but ~~more scenes, a broader range of melt pond fractions, and inclusion of wind information~~ the authors claim that more scenes with various sea ice types and incidence angles are needed to ~~confirm the findings.~~ develop a general propose f_{MP} model. Lack of wind information is also limiting the relevance of the study.

In summary, the main achievements on f_{MP} retrieval with SAR come from *dual polarimetric* C-band studies on land-fast FYI~~or MYI. Few studies have investigated other frequencies, and little attention has been paid to drifting FYI , an ice type~~ . The potential of f_{MP} retrieval with polarimetric X-band SAR has only been explored in one single study by Han et al. (2016), focusing on MYI. Hence, there is a need for more studies on the influence of f_{MP} on polarimetric X-band SAR imagery. As MYI and land-fast FYI have been the main focus in previous studies, there is also a

need to expand to other sea ice types. Drifting FYI is becoming more prominent in the Arctic with the recent shift to a thinner, more seasonal, and more mobile sea ice cover (Perovich et al., 2015), and the polarimetric SAR signature of f_{MP} in drifting FYI needs more attention.

The objective of this study is to investigate the potential of melt pond fraction retrieval from level drifting FYI with ~~dual polarimetric~~ dual-polarisation X-band satellite SAR. A data set consisting of four high resolution dual-polarisation TerraSAR-X satellite scenes, combined with melt pond fraction retrieved from a helicopter-borne camera system forms the basis of the study. TerraSAR-X offers very high resolution multi-polarimetric data, with a strong sensitivity to micro-scale surface roughness due to the high frequency. Both the high resolution and sensitivity to surface roughness can be advantages in f_{MP} investigations. The data were collected north of Svalbard in summer 2012. We explore the correlation between f_{MP} and different polarimetric SAR features extracted from the HH and VV channels. Based on the results, we suggest two simple empirical ~~models~~ regression fits for f_{MP} estimation adjusted to an intermediate and a low-wind speed case. The influence and limitations related to wind conditions, incidence angle, noise floor, scale and surface roughness are discussed in light of the results.

2 Melt ponds in SAR imagery

The signature of melt ponds in SAR imagery depends on both melt pond properties and radar parameters. Wind at the sea ice surface changes the surface roughness of the melt ponds, and hence their SAR backscatter signature and contrast to the surrounding sea ice. The influence of wind is dependent on fetch length, depth of the ponds, orientation of the ponds and the topography of the surrounding sea ice (Scharien et al., 2012, 2014b). During very calm conditions, the SAR signal of melt ponds is mainly specular. This occurs at wind speeds of $2-3$ m/s in 10 m height (U_{10}) in C-band, in agreement with findings for ocean surfaces (~ 2.0 m/s at $0°C$) (Donelan and Pierson, 1987; Scharien et al., 2012, 2014b). A similar threshold in X-band equals ~ 2.8 m/s (Donelan and Pierson, 1987). Refrozen ponds suppress the wind wave surface roughness induced on open ponds, and yield a signature closer to newly formed sea ice (Yackel et al., 2007; Scharien et al., 2014b, a). The size distribution of melt ponds also affects their SAR signature. Ponds smaller than the SAR resolution return a signal mixed with sea ice and possibly leads, while very large melt ponds could fill a resolution cell. Choice of SAR resolution and speckle smoothing window size could hence affect the SAR f_{MP} signature. The coverage of melt ponds varies during the melt season, starting out with a high fractional cover, and reducing as the ponds drains. At the end of the melt season, the melt ponds refreezes. This evolution is mirrored by a seasonal variation in the sea ice SAR signature (Barber et al., 2001).

The SAR signature of melt ponds changes with incidence angle of the satellite. Scharien et al. (2012) found a larger decrease in C-band SAR intensity (σ^0) with increasing incidence angle for

melt ponds than for sea ice. In contrast to sea ice, σ^0_{HH} decreased more than σ^0_{VV} for melt ponds. The most suitable incidence angle ranges for f_{MP} retrieval is method dependent. SAR frequency also influences the melt pond signature (Kern et al., 2010). ~~Observed surface roughness increases with increasing frequency, making~~ X-band is more sensitive to small-scale surface roughness than C-band, as the effect of surface roughness depends on radar wavelength. In addition, the sea ice volume penetration depth decreases with increasing frequency, leading to less volume scattering from sea ice at higher frequencies.

Several dual-polarimetric SAR features have been suggested for f_{MP} retrieval from SAR, utilizing different expected relations to physical properties of sea ice and melt ponds (Scharien et al., 2012, 2014a; Fors et al., 2015; Han et al., 2016). ~~Six~~ Eight of these features are included in our study and are described in the following subsection.

2.1 Polarimetric SAR features

For a fully polarimetric SAR system, which transmits and receives both horizontally (H) and vertically (V) polarised waves, the scattering matrix can be written as

$$\boldsymbol{S} = \begin{bmatrix} S_{HH} & S_{VH} \\ S_{HV} & S_{VV} \end{bmatrix} = \begin{bmatrix} |S_{HH}|e^{j\phi_{HH}} & |S_{VH}|e^{j\phi_{VH}} \\ |S_{HV}|e^{j\phi_{HV}} & |S_{VV|}e^{j\phi_{VV}} \end{bmatrix}, \tag{1}$$

where $|\cdot|$ and ϕ_{xx} denote the amplitude and the phase of the measured complex scattering coefficients, respectively (Lee and Pottier, 2009). Assuming reciprocity ($S_{HV} = S_{VH}$), the Pauli basis scattering vector, $\boldsymbol{k}$, can be extracted from $\boldsymbol{S}$ as

$$\boldsymbol{k} = \frac{1}{\sqrt{2}} \begin{bmatrix} S_{HH} + S_{VV} & S_{HH} - S_{VV} & 2S_{HV} \end{bmatrix}^{\dagger}, \tag{2}$$

where † denotes the transpose operator (Lee and Pottier, 2009). In our study, we are only utilizing the co-polarisation channels (HH and VV), and so the scattering vector reduceds to

$$\boldsymbol{k} = \frac{1}{\sqrt{2}} \begin{bmatrix} S_{HH} + S_{VV} & S_{HH} - S_{VV} \end{bmatrix}^{\dagger}. \tag{3}$$

The sample coherency matrix, $\boldsymbol{T}$, is defined as the mean Hermitian outer product of the Pauli basis scattering vector:

$$\boldsymbol{T} = \frac{1}{L} \sum_{i=1}^{L} \boldsymbol{k}_i \boldsymbol{k}_i^{*\dagger}, \tag{4}$$

where $\boldsymbol{k}_i$ is the single-look complex vector corresponding to pixel i, L is the number of scattering vectors in a local neighborhood, and $*$ denotes the complex conjugate (Lee and Pottier, 2009). Similarly, in the dual-polarisation case, the Lexicographic basis scattering vector, $\boldsymbol{s}$, can be written as

$$\boldsymbol{s} = \begin{bmatrix} S_{HH} & S_{VV} \end{bmatrix}^{\dagger}. \tag{5}$$

Based on $\boldsymbol{s}$, the sample covariance matrix, $\boldsymbol{C}$, is defined as

$$\boldsymbol{C} = \frac{1}{L}\sum_{i=1}^{L} \boldsymbol{s}_i \boldsymbol{s}_i^{*\dagger}, \tag{6}$$

where $\boldsymbol{s}_i$ is the single look complex vector corresponding to pixel i (Lee and Pottier, 2009).

The SAR intensity (σ^0) is retrieved from a single polarisation channel, defined by the amplitudes of the complex scattering coefficients,

$$\sigma^0_{VV} = \langle |S_{VV}|^2 \rangle \text{ and } \sigma^0_{HH} = \langle |S_{HH}|^2 \rangle, \tag{7}$$

were $\langle \cdot \rangle$ denotes an ensemble average. The relation between these basic features and f_{MP} have been investigated in several studies (Jeffries et al., 1997; Yackel and Barber, 2000; Mäkynen et al., 2014; Kern et al., 2010; Kim et al., 2013). However, carrying information from one single polarisation channel only, makes them less robust than polarimetric features that hold information from several channels.

Co-polarisation ratio ($R_{VV/HH}$) has so far been the most promising SAR feature for f_{MP} extraction in C-band (Scharien et al., 2014a). It is defined as the ratio between the intensities of the co-polarisation complex scattering coefficients

$$R_{VV/HH} = \frac{\langle |S_{VV}|^2 \rangle}{\langle |S_{HH}|^2 \rangle}. \tag{8}$$

For smooth surfaces within the Bragg scatter validity region, $R_{VV/HH}$ depends only on the surface complex permittivity and local incidence angle, and is independent of surface roughness (Hajnsek et al., 2003). Both freshwater and saline melt ponds have considerably higher complex permittivity than sea ice, and $R_{VV/HH}$ has therefore been suggested for f_{MP} retrieval (Scharien et al., 2012, 2014b, a). The Bragg criterion is fulfilled for $ks_{RMS} < 0.3$, where k is the wavenumber and s_{RMS} is the root mean square height of the sea ice surface, describing its surface roughness. This corresponds to $s_{RMS} < 2.8$ mm in C-band, and $s_{RMS} < 1.4$ mm in X-band. The sea ice surface roughness was found to high to fill the criterion in studies north of Spitsbergen and in the Fram Strait (Beckers et al., 2015; Fors et al., 2016b), while Scharien et al. (2014b) found land-fast ice in the central Canadian Arctic Archipelago to fulfill the criterion at C-band, and partly at X-band. In the same study, melt ponds filled the criterion at wind speeds below 6.4 m/s in C-band, corresponding to ~ 5.5 m/s in X-band (Scharien et al., 2014b). When the Bragg criterion is exceeded, $R_{VV/HH}$ decreases with increasing surface roughness. $R_{VV/HH}$ increases with incidence angle, and Scharien et al. (2012) found incidence angles above 35° to be most appropriate for f_{MP} retrieval based on $R_{VV/HH}$ in C-band.

Relative kurtosis (RK) is a statistical measure of non-Gaussianity, which describes the shape of the distribution of scattering coefficients in SAR scenes. It has previously been used for sea ice segmentation (Moen et al., 2013; Fors et al., 2016a). It is defined as Mardia's multivariate kurtosis

of a sample, divided by the expected multivariate kurtosis of a complex normal distribution

$$\mathrm{RK} = \frac{1}{L}\frac{1}{d(d+1)}\sum_{i=1}^{L}\left[\mathbf{s}_i^{*\dagger}\mathbf{C}^{-1}\mathbf{s}_i\right]^2, \tag{9}$$

where d is the number of polarimetric channels (Mardia, 1970; Doulgeris and Eltoft, 2010). It has a potential in f_{MP} retrieval as it is sensitive to mixtures of surfaces. At C-band, RK was found significantly correlated to f_{MP} over iceberg-fast sea ice in the Fram Strait (Fors et al., 2015).

Entropy (H) is a part of the $H/A/\overline{\alpha}$ polarimetric decomposition, based on the eigenvectors and eigenvalues of $\boldsymbol{T}$, describing SAR scattering mechanisms. H is a measure of the randomness of the scattering processes, and is defined as

$$H = -\sum_{i=1}^{d} p_i \log_d p_i, \tag{10}$$

where p_i is the relative magnitude of each eigenvalue

$$p_i = \frac{\lambda_i}{\sum_{k=1}^{d}\lambda_k}, \tag{11}$$

and λ_i is the i^{th} eigenvalue of $\boldsymbol{T}$ ($\lambda_1 > \lambda_2$) (Cloude and Pottier, 1997). Only the co-polarisation channels (HH and VV) are included in our study ($d = 2$), and a dual polarisation version of the entropy, denoted H', is therefore used (Cloude, 2007; Skrunes et al., 2014). $H' = 0$ indicates a single dominant scattering mechanism, while $H' = 1$ indicates a depolarized signal. In the case of dual polarisation, H' and anisotropy represent the same information as they both only depends on λ_1 and λ_2, and anisotropy is therefore not included in our study.

The alpha angle of the largest eigenvalue (α_1') describes the type of the dominating scattering mechanism. It is expressed as

$$\alpha_1' = \cos^{-1}\frac{|x_1|}{|v_1|}, \tag{12}$$

where x_1 is the first element of the largest eigenvector, and $|v_1|$ is the norm of the first eigenvector (Lee and Pottier, 2009). The feature can be written as a function of $R_{VV/HH}$ for slightly rough surfaces, and will then increase with increasing complex permittivity (van Zyl and Kim, 2011).

Co-polarisation correlation magnitude ($|\rho|$) is defined as

$$|\rho| = \left|\frac{\langle S_{\mathrm{HH}} S_{\mathrm{VV}}^{*}\rangle}{\sqrt{\langle S_{\mathrm{HH}} S_{\mathrm{HH}}^{*}\rangle\langle S_{\mathrm{VV}} S_{\mathrm{VV}}^{*}\rangle}}\right|, \tag{13}$$

and describes the degree of correlation between the co-polarisation channels (Drinkwater et al., 1992). A perfect correlation returns unity, while depolarisation of the signal will reduce the magnitude. Complex surfaces, multiple scattering surface layers and/or presence of system noise could depolarize the signal (Drinkwater et al., 1992).

Phase difference ($\angle\rho$) is expressed as (Drinkwater et al., 1992)

$$\angle\rho = \angle\left(\left\langle S_{\mathrm{HH}} S_{\mathrm{VV}}^{*} \right\rangle\right). \tag{14}$$

As the relative phase of the co-polarisation waves is changed in every scattering event, the mean and standard deviation of $\angle\rho$ are related to the scattering history (Eom and Boerner, 1991; Drinkwater et al., 1992). Han et al. (2016) found H, α_1', $|\rho|$, and $\angle\rho$ to give useful information for f_{MP} retrieval at X-band.

3 Methods

3.1 Study region and sea ice conditions

The ICE2012 campaign took place on drifting FYI north of Svalbard, in the southwestern Nansen Basin (Fig. 1), where the research vessel R/V Lance was moored up to an ice floe for eight days. The sea ice cover in the area is generally dominated by first- or second-year ice with only moderate amounts of deformation (Renner et al., 2013). While large seasonal variability exists in the area, summer ice thickness has been fairly stable since 2007. However, Renner et al. (2013) found further indicators for a trend towards younger sea ice in the region. Little deformation and dominance of young ice leads to relatively low sea ice surface roughness, with a root mean square height of around or less than 0.1 m in the region (Beckers et al., 2015). Substantial snow cover can accumulate during spring, however, during the summer season, the snow melts completely contributing to extensive melt pond formation.

During the ICE2012 campaign, regular sea ice thickness and melt pond surveys were performed on the ice and from helicopter. Modal ice thickness in the region was less than in previous years with 0.7 to 0.9 m (Divine et al., 2015). The very close drift ice was fairly level with less than 10% deformed ice. Sea ice surface roughness retrieved from the floe by R/V Lance is given in Table 3. The surface roughness values are expected to be representative for the whole study region, as the sea ice in the area was found to be very uniform (Hudson et al., 2013; Divine et al., 2015). The values also agree well with values derived from laser altimeter observations by Beckers et al. (2015).

At the time of the campaign, all snow had melted and extensive networks of melt ponds led to an average f_{MP} of 26% of the sea ice area (Divine et al., 2015). The melt ponds were mostly whithin 15 to 30 cm deep, however, extensive melt led to some ponds having melted through the ice slab. The water in the pond networks was therefore mostly saline.

Hudson et al. (2013) report an average thinning of the sea ice next to R/V Lance of over 17 cm between 28 July and 2 August which to a large degree can be explained by absorption of atmospheric and oceanic heat by the ice. Air temperatures were varied little between -1 to $1.5°C$. Combined with the oceanic heat flux, the ice was therefore in continuous melt even at nighttime. Meteorological conditions were dominated by heavy cloud cover with only short spells of incomplete or thin cloud

cover. Ice cores were taken every other day between 27 July and 2 August with an additional core on 28 July for chemical analysis. They confirm the presence of a consistent 4 to 5 cm thick surface scattering layer of white, granular, deteriorated ice. Temperature profiles through the ice were fairly stable with vertical variations between near $0°C$ at the surface to -1 to $-1.3°C$ at the bottom. Salinity measurements show very low values in the upper 20 cm with salinities of less than 1 psu and increasing to 3 to 4 psu near the bottom, in agreement with the advanced stage of melt of the ice cover.

3.2 Data set

In situ and helicopter-borne measurements from ICE2012 are combined with four high-resolution TerraSAR-X (TS-X) satellite scenes. The satellite scenes are StripMap mode acqusitions, with a HH-VV channel combination (see Table 1 and Fig. 1). The scene labeled T1 was acquired in descending orbit, while T2-T4 were acquired in ascending orbits. All scenes were converted to ground range and radiometrically calibrated to σ^0. The ~~calibration was performed both with and without subtraction of the~~ noise equivalent σ^0 (NESZ) ~~.~~ was then subtracted. The absolute radiometric calibration accuracy of TSX is 0.6 dB (Airbus Defence and Space, 2013). For comparison with f_{MP} retrieved from helicopter-borne data, the scenes were geocoded with ESA's Sentinel-1 toolbox, SNAP (European Space Agency, 2016). All analysis were, however, performed in SLC range and azimuth coordinates. Open water areas were not included in our study. For each satellite scene, these areas were masked out with a simple binary mask. The mask was created by filtering the scenes with a 13×13 pixels averaging sliding window, and manually setting a lower sea ice threshold value on σ^0_{HH} in each scene (-18 dB,-17 dB,-16 dB and -18 dB, for T1-T4 respectively). Regions with less than 750 pixels ($\sim 5000\ m^2$) were merged into the surrounding region (open water or sea ice) to smooth the mask.

A stereocamera system (ICE stereocamera system) was mounted in a single enclosure outside the helicopter during ICE2012 (Divine et al., 2016, in review). The system consisted of two cameras (Canon 5D Mark II), combined with GPS/INS (Novatel) and a laser altimeter. f_{MP} was retrieved from downward-looking images captured by one of the cameras during five helicopter surveys performed between 31 July and 2 August 2012 (see Table 2 and Fig. 1). The footprint of the images was about 60×40 m for a typical flight altitude of about 35 m, and the images were not overlapping. A full description of the method is given in Divine et al. (2015). In our study, f_{MP} was calculated from the processed images without sea water fraction (~ 5700 images), to better match the sea ice mask. This excluded melt pond fractions from the ice edges and small floes, resulting in a slightly higher f_{MP} than that obtained in Divine et al. (2015).

The ICE stereocamera system was also used to investigate sea ice surface topography at the floe where R/V Lance was anchored. For this purpose, the cameras shot sequentially with a frequency of 1 Hz to ensure sufficient overlap between subsequent images during the flights. Using photogrammetric technique, the sequences of overlapping images were used to construct a digital terrain model

(DTM) of the sea ice surface. DTMs were generated for five selected segments of the ICE12 ice floe with a spatial resolution of 2 cm. Surface roughness, in form of root mean square height of the sea ice surface (s_{RMS}), was estimated from the DTMs using random sampling to account for spatial auto-correlation. Only grid nodes above the water level were used. The accuracy of the retrieved s_{RMS} were ± 4 cm according to *in situ* measurements from two test areas. A full description of the method is given in Divine et al. (2016, in review).

An automatic weather station located at the floe where R/V Lance was moored during ICE2012 measured wind speed and air temperature 2 m above the sea ice surface(Hudson et al., 2013). Wind speed (U_2) was measured with a three-dimensional ultrasonic anemometer (Campbell Scientific Inc., CSAT3), and air temperature was measured with a temperature probe (Vaisala, HMP155) in an unventilated radiation shield. Tab. 1 presents air temperature and 10 minutes averaged wind speed at the time of the satellite acquisitions.

3.3 Design of study

An easy recognizable sea ice floe present in two of the investigated satellite scenes (T3 and T4) is the main focus of our study (see Fig. 2). The floe had a diameter of ~ 3.6 km, and a collection of 43 images was captured across the floe during the 2$^{\text{nd}}$ helicopter flight on 2 August 2012 (see Tab. 2). The time offset between the flight and acquision of T4 was ~ 40 minutes. The position of the helicopter images had to be corrected for sea ice drift to retrieve co-location between the images and the floe captured in T4. As a first step, the image center coordinates were shifted according to drift information from GPS tracks of R/V Lance, positioned ~ 25 km south of the floe at the time of acquisition. Second, the track was manually adjusted by fitting the helicopter images with ground features, such as ice edges and areas with open water. Co-location of the helicopter images and the floe in T3 was based on the one of T4. The maximum error of the co-location was estimated to be 7 m lengthwise and crosswise the flight direction, resulting in a maximum possible areal offset of 27% between the satellite scene and each helicopter image. After co-location, mean and standard deviation of the polarimetric SAR features were calculated for the pixels underlying each of the helicopter images.

The statistical dependence between the extracted SAR features and the corresponding f_{MP} retrieved from each of the 43 helicopter images was evaluated with the non-parametric Spearman's rank correlation coefficient (r). For a sample size of n images, r is defined as

$$r = 1 - \frac{6 \sum d_i^2}{n(n^2 - 1)}, \tag{15}$$

where d_i is the difference in paired rank number i (Corder and Foreman, 2009). Rank ties are assigned a rank equal to the average of their position in the ascending order of the values. The coefficient takes values between -1 and 1, where values of ± 1 correspond to full correlation, while 0 corresponds to no correlation. A negative sign indicates an inverse relationship. ~~The calculation of r~~

assumes of Spearman's correlation coefficient assumes a monotonic relationship, and is . It is used instead of Pearson's linear correlation coefficient, to allow for non-linear correlations. It is also less sensitive to outliers than Pearson's linear correlation coefficient.

Two empirical models regression fits were proposed from the correlation results, representing an intermediate and a low-wind case. A least squares linear fit with bisquare weights was used to construct the models regression fits (Hoaglin et al., 1983). The models regression fits were applied to the full area of the floe in T3 and T4, and to the full area of the four satellite scenes included in the study (T1-T4). The estimated f_{MP} distributions were compared and evaluated towards the global empirical f_{MP} distribution retrieved from the helicopter flights included in the study (see bottom entries Tab. 2). Scale sensitivity was tested by using a range of different smoothing window sizes (13×13 to 51×51 pixels) in the f_{MP} estimation. Incidence angle correction was applied to the scenes for a better comparison, employing the following equation (Kellndorfer et al., 1998)

$$\sigma^0_{corr} = \sigma^0 \frac{sin(\theta)}{sin(\theta_{ref})}, \tag{16}$$

where σ^0 is the original backscatter coefficient, θ is the center incidence angle of the scene to be corrected, and θ_{ref} is the reference incidence angle of scene T4. The correction was only applied in the low-wind case, as it canceled in the intermediate wind case due to the use of a co-polarisation ratio.

4 Results

4.1 Sea ice conditions

During the ICE2012 campaign, regular sea ice thickness and melt pond surveys were performed on the ice and from helicopter. Modal ice thickness in the region was less than in previous years with 0.7 to 0.9 m (Divine et al., 2015). The very close drift ice was fairly level with less than 10% deformed ice. Sea ice surface roughness retrieved from the floe by R/V Lance is given in Table 3. The surface roughness values are expected to be representative for the whole study region, as the sea ice in the area was found to be very uniform (Hudson et al., 2013; Divine et al., 2015). The values also agree well with values derived from laser altimeter observations by Beckers et al. (2015).

At the time of the campaign, all snow had melted and extensive networks of melt ponds led to an average f_{MP} of 26% of the sea ice area (Divine et al., 2015). The melt ponds were mostly whithin 15 to 30 cm deep, however, extensive melt led to some ponds having melted through the ice slab. The water in the pond networks was therefore mostly saline.

Hudson et al. (2013) report an average thinning of the sea ice next to R/V Lance of over 17 cm between 28 July and 2 August which to a large degree can be explain by absorption of atmospheric and oceanic heat by the ice. Air temperatures were mostly around freezing point varying only little

between -1 to $1.5°C$. Meteorological conditions were dominated by heavy cloud cover with only short spells of incomplete or thin cloud cover. Ice cores were taken every other day between 27 July and 2 August with an additional core on 28 July for chemical analysis. They confirm the presence of a consistent 4 to 5 cm thick surface scattering layer of white, granular, deteriorated ice. Temperature profiles through the ice were fairly stable with vertical variations between near $0°C$ at the surface to -1 to $-1.3°C$ at the bottom. Salinity measurements show very low values in the upper 20 cm with salinities of less than 1 psu and increasing to 3 to 4 psu near the bottom, in agreement with the advanced stage of melt of the ice cover.

4.1 Correlation between polarimetric SAR features and f_{MP}

Correlation coefficients (r) between f_{MP} retrieved from the 43 helicopter images of the investigated floe, and the mean and standard deviation of the polarimetric SAR features extracted from the corresponding areas in scenes T3 and T4, are presented in Table 4. Values significant within a 95% confidence interval are highlighted in bold, and values in parentheses show results after before NESZ subtraction of the signal was included in the calibration. In scene T3, $R_{VV/HH}$ shows the strongest correlation to f_{MP}, both with and without NESZ subtraction. In addition, the mean of α_1 is significantly correlated to f_{MP} when the NESZ subtraction is included in the calibration. None of the other investigated SAR features are significantly correlated to f_{MP} in scene T3. In scene T4, the mean values of most of the features, and some of their standard deviation values are σ^0_{HH}, σ^0_{VV} and $R_{VV/HH}$ are significantly correlated to f_{MP}. The , the strongest correlation is found between for σ^0_{VV} and . Some of the standard deviation values are also correlated to f_{MP}. Introducing Without NESZ subtraction in the calibration, however, reduces the number of correlations, indicating almost all features are correlated to f_{MP}. The large difference before and after NESZ subtraction indicates that the signal is close to, or reaching the noise floor.

Figure 3 confirms the low signal-to-noise ratio in T4. We show the 10, 25, 50, 75 and 90 percentiles of σ^0_{HH} (dB) and σ^0_{VV} (dB) retrieved for four different f_{MP} intervals on the floe present in scene T3 (top) and T4 (bottom), combined with the noise floor of the HH and VV channels. In T3, less than 10% of the signal is below the noise floor (~ -25 dB). Both σ^0_{HH} and σ^0_{VV} are increasing with f_{MP}. σ^0_{VV} has the steepest increase, confirming an increase in $R_{VV/HH}$ with f_{MP} (Tab. 4). In scene T4, the backscatter signal is weaker and noise floor is higher than in scene T3 (~ -21 dB), both due to the higher incidence angle of scene T4 (see Tab. 1). This brings as much as 25% of the signal below the noise floor. The strength of the signal decreases with f_{MP}, implying specular reflection from the melt ponds, supported by the low wind speed (0.6 m/s) at acquisition of scene T4 (see Tab. 1). The difference between σ^0_{HH} and σ^0_{VV} is decreasing with f_{MP}, confirming an inverse relation between $R_{VV/HH}$ and f_{MP} in T4 (Tab. 4). In scene T1 and T2, the noise floors are ~ 23 dB, leaving $\sim 15\%$ of the signal below the noise floor.

The melt ponds affect the polarimetric signatures in scene T3 and T4 differently (Table 4 and Fig. 3), mainly due to different wind conditions, but also due to different incidence angles and noise floors. ~~Based on these results, two empirical models for~~ In the following, we look closer into the feature displaying the strongest correlation to f_{MP} ~~estimation are presented in the following. One model is retrieved from the intermediate-wind case seen in cene~~ in each of the scenes, $R_{VV/HH}$ in T3 ~~, and one from the low-wind case seen in scene~~ and σ^0_{VV} in T4.

4.2 Intermediate-wind case

In the intermediate-wind case of scene T3, $R_{VV/HH}$ was found to be the SAR feature with the strongest correlation to f_{MP}. Combining f_{MP} retrieved from the 43 helicopter images covering the investigated floe with $R_{VV/HH}$ extracted from the corresponding areas in scene T3, we see an increase in $R_{VV/HH}$ with f_{MP} in Fig. 4, as well as a large variability between the samples. Grey dots correspond to areas with some degree of sea ice deformation, while blue dots correspond to areas with completely level ice. Deformation information is extracted from visual inspection of the helicopter images. The partly negative values of $R_{VV/HH}$ ~~implies~~ imply that $\sigma^0_{HH} > \sigma^0_{VV}$~~,~~ ~~especially in the areas with low f_{MP}. From visual inspection of the helicopter images, some of the~~ . This might be a result of multiple scattering events in the sea ice volume or sea ice surface, possibly connected with sea ice deformation. A majority of the lowest $R_{VV/HH}$ values ~~origin from slightly deformed areaswith a surface roughness possibly exceeding the Bragg criterion~~are appearing in partly deformed areas. Areas with some degree of deformation also represent the lowest f_{MP}. A robust least squares linear fit ~~was used to construct an empirical model from the displayed relationship~~ is applied to the scatter plot, displaying a relationship of:

$$f_{MP}(R_{VV/HH}) = 0.49 \cdot R_{VV/HH}(dB) + 0.30. \tag{17}$$

The goodness of fit of the ~~model~~ regression is reflecting large sample variation, with ~~$r^2 = 0.21$~~ $R^2_{fit} = 0.21$ and $RMSE = 0.40$~~, but the model still provides a starting point for estimation of f_{MP}~~. This implies a weak correlation, corresponding well to the Spearman's correlation of 0.45 (Table 4). However, the co-location between the helicopter images and the sea ice floe contain some uncertainty (a maximum areal offset of 27%) possibly introducing a random error to the regression, resulting in an artificially low R^2_{fit}.

Applying the ~~model based~~ regression fit from on Eq. 17 to the full floe in scene T3 results in the ~~model~~ regression fit probability density distributions (PDFs) presented in the top panel of Fig. 5. The results are presented both for a 21×21 and a 51×51 pixels smoothing window. Empirical distributions of f_{MP} retrieved from the 43 images covering the floe (floe) and from images in all included flights (global), are also included in the figure. Statistics of the distributions are given in Tables 2 and 5. The empirical global distribution has a slightly higher mean than the empirical floe distribution. Due to the few samples of the floe distribution, we consider the global distribution more appropriate

for comparison with the ~~modeled~~ regression fit distributions. Employing the ~~model~~ regression fit with a 21×21 pixels smoothing window, equaling the areal size of the helicopter images, results in a mean close to the global empirical. The ~~modeled~~ regression distribution is however too wide compared to the empirical ones, reflecting the large sample variation seen in Fig. ~~5~~4. Speckle (noise like interference between scatterers within a resolution cell) in the SAR image might explain the wider distribution. Increasing the smoothing window size reduces speckle, and a better correspondence between the width of the ~~modeled~~ regression and empirical distributions is achieved by employing a 51×51 pixels window. The bottom panel of Fig. 5 displays f_{MP} estimated for the floe in T3 based on eq.17 with a 51×51 pixels window. Open water is masked out. The estimation shows a highly spatially variable f_{MP}, with few homogenous areas. Areas of deformed sea ice displayed with bright colors in Fig. 2 cannot be recognized, even if these areas are expected to have a lower melt pond fraction. ~~A further validation of the results is not possible based on the collected data.~~

Zooming in to the southern part of the area covered by the helicopter survey on the floe in T3, Fig. 6 displays f_{MP} estimated from Eq. 17 with the observed f_{MP} from the helicopter images overlaid. Two different pixels smoothing windows are shown (21×21 and 51×51). Note that the center pixel underlying each helicopter image frame would give the most representative value for comparison to the observed f_{MP}, as pixels closer to the frame contain a larger amount of information from outside the frame. The middle panel displays the mean estimated f_{MP} value for each frame together with the observed f_{MP} values along the track. The maps confirm some overlap between the estimated and observed f_{MP}, but also illustrates that there is room for improvement. The estimation with a 51×51 pixel smoothing window appears less variegated than the 21×21 estimation, and the range of the estimated f_{MP} values also corresponds better to those observed from the helicopter images in the 51×51 estimation.

Applying the ~~intermediate-wind model~~ regression fit from Eq. 17 with a 51×51 pixel window to the four full SAR scenes included in our study reveals a high correlation between the ~~modeled~~ regression fit distribution and the empirical global f_{MP} distribution for T3 (see Fig. 7 and Tables 2 and 5). On the full scene scale, the ~~model~~ regression fit manages to reproduce both the mean and the standard deviation of the global distribution representative for the area. Scene T1 and T2 are acquired at $\sim 8^\circ$ higher incidence angle than scene T3, and f_{MP} is slightly overestimated in these scenes. From Fig. 7, the overestimation is lower for scene T1 than for T2, possibly reflecting the low wind speed at acquisition of T1 (Tab 1). The least consistency between ~~model and~~ the regression fit distribution and the empirical distribution is, as expected, found for scene T4, confirming the results shown in Table 4 and Fig. 3.

4.3 Low-wind case

In the low-wind case of scene T4, σ^0_{VV} was found to have the strongest correlation to f_{MP} among the investigated SAR features. Combining f_{MP} retrieved from the 43 helicopter images covering the

floe with σ^0_{VV} extracted from the corresponding areas in T4, we see a decrease in σ^0_{VV} with f_{MP} in Fig. 8. A large variability between the samples can be observed. Grey dots correspond to partly deformed areas, while blue dots represent level ice. As for the intermediate wind case, ~~an empirical model was constructed using~~ a robust least square linear fit ~~to~~ was applied to the data to describe the relationship ~~:~~ between σ^0_{VV} and f_{MP}:

$$f_{MP}(\sigma^0_{VV}) = -0.32 - 52.83 \cdot \sigma^0_{VV}(dB) - 4.64 + 1.89. \quad (18)$$

Note that σ^0_{VV} is not in dB. Again, the goodness of fit of the ~~model reflects the high sample variability in Fig. 8, with $r^2 = 0.15$ and $RMSE = 0.63$, but we consider the model to provide a good starting point for estimation of f_{MP}~~regression is reflecting large sample variation, with $R^2_{fit} = 0.26$ and $RMSE = 0.0039$.

~~Modeled~~ Estimated f_{MP} PDFs based on ~~eq~~Eq. 18 for the full floe in scene T4 are presented in the top panel of Fig. 9 together with empirical distributions from the floe and from all flights included in the study. The ~~modeled~~ regression fit distributions give a good reproduction of the empirical mean (see Tables 2 and 5). As in the intermediate-wind case, a smoothing window of 51×51 pixels results in a distribution width closer to the empirical than a 21×21 pixels window. The σ^0_{VV}-based estimation of f_{MP} with a 51×51 smoothing window for the full floe in scene T4 result in a large spatial variability in f_{MP} (see bottom panel of Fig. 9). In contrast to the f_{MP} estimation based on $R_{VV/HH}$ for the floe in scene T3 (Fig. 5), the ~~low-wind model~~ estimation based on σ^0_{VV} partly manages to produce lower melt pond fraction in areas with deformed sea ice.

~~Investigating the low-wind model~~Figure 10 shows f_{MP} estimated from Eq. 18 with the observed f_{MP} from the helicopter images overlaid for two different pixels smoothing windows (21×21 and 51×51). Note that the center pixel underlying each helicopter image frame would give the most representative value for comparison to the observed f_{MP}. To illustrate this, the middle panel shows the mean estimated f_{MP} value for each frame together with the observed f_{MP} values along the track. In general, a good overlap between the estimated and observed f_{MP} can be seen, even though some scatter exists. As in Fig. 6, the estimation with a 51×51 pixel smoothing window appears less variegated than the 21×21 estimation, and the range of the estimated f_{MP} values also corresponds better to those observed from the helicopter images in the 51×51 estimation than to those in the 21 x 21 estimation.

Investigating the regression fit's capacity of estimating f_{MP} in the 4 full satellite scenes included in the study reveals that it is only applicable to give a good estimate in scene T4 (see Fig. 11 and Table 2 and 5)). In the three other scenes, it underestimates f_{MP}, and also introduces negative fractions. ~~An underestimation is expected for lower incidence angles, as~~ Incidence angle correction according to Eq. 16 is applied to the figure, accounting for σ^0_{VV} ~~decreases~~ decrease with incidence angle~~, but the magnitude of the underestimation is too large to be explained by the incidence angle dependency alone~~.

5 Discussion

The results of this study show that ~~retrieval of~~ f_{MP} influences the signature of several X-band polarimetric features. The strongest correlations were found for $R_{VV/HH}$ and σ^0_{VV}, where linear regression fits gave R^2_{fit} values of 0.21 and 0.26, respectively. These correlations are not strong enough for the results to be used directly in operational models. However, with improved methods and more satellite data added, our results imply a future potential in retrieving f_{MP} from X-band SAR~~is possible, but as~~. For comparison, the method developed for retrieval of f_{MP} from MODIS has R^2_{fit} values ranging from 0.28 to 0.45 (Rösel et al., 2012). As in C-band, parameters like wind speed, incidence angle, surface roughness, and SAR scale and resolution will affect the interpretation of the polarimetric melt pond signature of ~~an~~ a X-band SAR scene. In the following, these factors will be discussed based on the results.

Accurate information about wind speed at the time of scene acquisition is crucial in f_{MP} retrieval from SAR. In scene T3, the intermediate wind speed at acquisition ($U_2 = 6.2$ m/s) allowed for backscatter from the melt ponds, making use of $R_{VV/HH}$ for f_{MP} estimation possible. Scharien et al. (2014b) finds that the Bragg criterion is exceeded for melt ponds at wind speeds above $U_{10} =\sim 5$ m/s in X-band, reducing the expected correlation between $R_{VV/HH}$ and f_{MP} above this wind speed. This indicates that even better results could be achieved at lower wind speeds, but it also leaves a very narrow wind speed interval for melt pond retrieval with X-band SAR. Scene T4 represents a low wind speed situation ($U_2 = 0.6$ m/s), and our results indicate specular reflection from the melt ponds in this case, disrupting the use of polarimetric SAR features for melt pond estimation as the melt pond signal is too weak. This is in agreement with findings in Scharien et al. (2012, 2014b). However, the lack of backscatter from the melt pond surfaces compared to the sea ice could potentially be used for f_{MP} retrieval utilizing σ^0. This is confirmed by Han et al. (2016), suggesting σ^0 to be a key feature in f_{MP} estimation for MYI in X-band during calm winds. On the other hand, our results deviate from findings in C-band, where no correlation was found between σ^0_{HH} and f_{MP} at low wind speeds by Yackel and Barber (2000).

Medium to high incidence angles ($> 35°$) have been found most suitable for $R_{VV/HH}$-based retrieval of f_{MP} in C-band (Scharien et al., 2012, 2014b). In our study we found a significant correlation between $R_{VV/HH}$ and f_{MP} at an incidence angle of 29° (T3), ~~indicating that~~ demonstrating that f_{MP} has an impact on polarimetric X-band SAR signatures also at lower incidence angles~~might be used for f_{MP} estimation, at least in X-band~~. Scene T1 and T2 are acquired at higher incidence angles (36.9° and 37.9°) than T3. In these two scenes, f_{MP} is overestimated by the $R_{VV/HH}$-based ~~model~~ regression fit developed for scene T3. This is consistent with Scharien et al. (2014b), showing an increase in $R_{VV/HH}$ with increasing incidence angle for melt ponds in C-band. In the same study, $R_{VV/HH}$ for bare ice was not found to increase with incidence angle. The difference in ~~modeled~~ estimated f_{MP} between scene T1 and T2 is most likely related to the low wind speed in T1, which is below the expected wind speed limit for f_{MP} estimation based on $R_{VV/HH}$ in both

C and X-band (Scharien et al., 2012, 2014b). However, the different acquisition geometry observed in Fig. 1 could also play a role. At an incidence angle of 44°, a considerable part of the backscatter signal was below the noise floor in our study. The low signal-to-noise ratio of TerraSAR-X limits f_{MP} retrieval based on $R_{VV/HH}$ at high incidence angles, leaving the suitable range of incidence angles smaller than for Radarsat -2 (Scharien et al., 2014a). The accuracy of f_{MP} estimation based on σ^0_{VV} is also strongly dependent on incidence angle, as σ^0_{VV} in general decreases with increasing incidence angle for sea ice. The underestimation of f_{MP} in scenes T1-T3 ~~, can partly be explained by lower incidence angles, but the~~ is likely related to higher wind speeds at ~~acquisition of these scenes likely also prevent good estimates of f_{MP} based on σ^0_{VV}~~ the time of acquisition.

The Brag criterion ($ks < 0.3$) is exceeded when $s_{RMS} > 1.4$ mm in X-band. The surface roughness estimations performed during the ICE2012 campaign indicates that the sea ice in the study region exceeds this criterion, introducing a roughness dependency of $R_{VV/HH}$. This is in agreement with previous findings in the study region (Beckers et al., 2015), but deviates from findings reported by Scharien et al. (2014b), where fast ice at the Central Canadian Archipelago partly filled the criterion in X-band. From the helicopter images, some of the very low $R_{VV/HH}$ values observed at the investigated floe in scene T3 were from slightly deformed areas, possibly explaining the negative ratios. However, no general trend in low $R_{VV/HH}$ values in deformed areas was found in our study. ~~Sea ice deformation may also~~ Multiple scattering events in the sea ice surface and sea ice volume may also have contributed to the large sample variations observed in ~~Fig~~Figs. 4 and 8. Detailed surface roughness measurements combined with f_{MP} observations are needed to further investigate the influence of sea ice surface roughness on f_{MP} based on $R_{VV/HH}$.

The smoothing window size used for direct comparison between f_{MP} retrieved from the helicopter images and the polarimetric SAR features was appointed by the areal coverage of the helicopter images in our study. However, a 40×60 m window (corresponding to 21×21 pixels) might not be the ideal scale of investigation. Advancing the ~~empirical models~~ regression fits suggested in our study to the full floe or full scenes with a larger window (51×51 pixels) gave better reproductions of the width of the f_{MP} distribution retrieved from the helicopter images. A larger window size reduces the amount of speckle in the SAR scenes, which ~~probably~~ possibly explains the improvement. Even larger window sizes were used in Scharien et al. (2014a), estimating f_{MP} based on $R_{VV/HH}$ in a 7.5×7.5 km grid from C-band Radarsat-2. Opposite to this, Han et al. (2016) found a 15×15 pixels window to give the best estimate of mean f_{MP} based on a combination of several SAR features in a TerraSAR-X scene. In climate applications, f_{MP} estimation from a full scene is more applicable than estimation from small areas within the scene. The large sample variability observed in Fig. 4 might therefore be negligible, as long as the $R_{VV/HH}$-based ~~model~~ regression fit produces a good ~~full scene~~ estimate of the mean f_{MP} for a larger area. A wider study of the influence of scale on SAR f_{MP} retrieval is needed in the future.

In addition to $R_{VV/HH}$, five other dual-polarimetric SAR features were included in our study~~,~~ after NESZ subtraction most of these showed no statistical significant relationship to f_{MP} in our data set. This is also an important result, implying useful knowledge for instance in classification of summer sea ice based on X-band imagery. The statistical feature RK showed a promising relation to f_{MP} in C-band on fast ice in the Fram Strait (Fors et al., 2015), but no relation was found in our investigation. Lack of the HV-channel, or less dominant height difference between ponds and sea ice could both possibly explain the absence of correlation. H' and α'_1 were found significantly correlated with f_{MP} in scene T4 and T3, respectively. In scene T4, the correlation to H' disappeared when NESZ subtraction was included in the calibration. This indicates that the correlation only reflected the low signal-to-noise ratio of the scene, as has previously been described in oil/water discrimination (Minchew et al., 2012). In scene T3, the correlation between f_{MP} and α'_1 is likely a result of the expected relation between α'_1 and $R_{VV/HH}$ (van Zyl and Kim, 2011). The correlations found between f_{MP} and mean and standard deviations of $|\rho|$ and $\angle\rho$ in scene T4 are, as for H', most likely related to the low wind speed and low signal-to-noise ratio of the scene. ~~$|\rho|$,~~

The findings in our study deviate from the findings of Han et al. (2016), where σ^0_{HH}, $\angle\rho$ and α'_1 were found ~~important for f_{MP} retrieval in the~~ to be the most prominent polarimetric features in separating melt ponds, sea ice and open water in high resolution X-band SAR ~~scene investigated by Han et al. (2016) , but lack of exact wind information~~ imagery. Differences in sea ice type, sea ice surface roughness, wind conditions and SAR incidence angle could possibly explain why different polarimetric features are sensitive to f_{MP} in the two studies. The methods of the two studies are also slightly different, as Han et al. (2016) classify each pixel into melt pond, sea ice or open water, while our study focuses on mixtures of melt ponds and sea ice. Exact wind information lacks in Han et al. (2016), but the wind speed is expected to be low. This could explain why σ^0_{HH} contributes strongly in f_{MP} estimation, and is then in accordance to our findings. The diverging results in the two studies emphasize the need of investigating melt ponds impact on SAR imagery under different conditions and for a variety of sea ice types. It also stresses the importance of supplementary measurements of parameters like wind speed and sea ice surface roughness.

The correlations found in our study are not very strong. The weak to moderate correlations might suggest a limited sensitivity to f_{MP} in ~~the study prevent a further comparison to our results.~~ X-band SAR imagery, but they could also reflect limitations in the data set. The co-location between the helicopter images and the SAR imagery is estimated to have a possible offset of at most 27%, potentially introducing a large random error into our investigation, lowering the correlation values. A larger degree of smoothing than the area covered by the helicopter images allows for might also be needed to improve the results. The absolute radiometric accuracy of TSX scenes could also influence the results of our study, but this influence is expected to be very small compared to other uncertainties. All the above-mentioned issues should be addressed in future studies.

6 Conclusions

Melt ponds play an important role in the sea-ice-ocean energy budget, but the evolution of melt pond fraction (f_{MP}) through the melt season is poorly monitored. Satellite-borne polarimetric SAR has shown promising results for f_{MP} retrieval in C-band, but few studies have investigated the opportunities in X-band. In this study we demonstrate ~~a significant relation~~ statistically significant relations between f_{MP} and several polarimetric SAR features on drifting FYI in X-band, based on helicopter-borne images of the sea ice surface combined with four dual polarimetric SAR scenes. The study reveals a prospective potential for f_{MP} estimation from X-band SAR, but also stresses the importance of including wind speed and incidence angle in a ~~prospective~~ future robust f_{MP} retrieval algorithm. ~~In the future, f_{MP} retrieved from X-band SAR~~ Such an algorithm could supplement optical methods, and be used as a tool in climate applications, both as input in climate models and in studies of melt pond evolution mechanisms.

$R_{VV/HH}$ was found to be the most promising SAR feature for f_{MP} estimation in our study, in agreement with previous findings in C-band. The theoretical range of suitable wind speeds (< 5 m/s) and sea ice surface roughnesses ($s_{RMS} < 1.4$ mm) for f_{MP} extraction based on $R_{VV/HH}$ are slightly more limited in X-band than in C-band, but our results show that ~~one can use $R_{VV/HH}$ for~~ f_{MP} ~~estimation even if~~ also influences the X-band SAR signature when these criteria are partly exceeded. The high noise floor of TerraSAR-X also restricted use of scenes with incidence angles above $\sim 40°$, while an incidence angle of $29°$ gave ~~good~~ better results. At very low wind speeds (0.6 m/s), the backscatter signal from the melt ponds became too low for f_{MP} retrieval based on ~~$R_{VV/HH}$~~polarimetric features. In that case, σ^0_{VV} was found suitable for f_{MP} estimation. ~~All in all~~In the future, use of X-band scenes can possibly increase the total amount of SAR data accessible for f_{MP} retrieval, despite their limitations compared to C-band scenes.

An extended amount of *in situ* and airborne measurements together with satellite scenes are needed to establish robust f_{MP} estimation algorithms for X-band SAR. Information about wind speed is crucial for f_{MP} retrieval, and can be retrieved from existing meteorological models or autonomous buoys measuring wind speed, where no ship or camp is present. ~~Co-location~~ Challenges in co-location of airborne observations and SAR imagery ~~challenged~~ limited coordinated use of existing data in our study ~~. A possible offset in location between the helicopter images and the investigated SAR scenes represents a major source of uncertainty~~ and introduced uncertainties in our results, possibly ~~introducing too~~ causing artificially low correlation values~~and a large RMSE of the empirical models~~. Better co-location, for instance through corner reflectors or GPS senders located in the specific study area, should be aimed for in future studies. With a shift towards more seasonal drifting FYI, it is important to include this sea ice type in the studies, despite difficulties in comparing *in situ* and airborne measurements with satellite SAR scenes during drift.

Our study only investigates a few SAR scenes under similar sea ice conditions, and the ability of the suggested ~~models~~ regression fits to predict changes in f_{MP} is not included. This is an important

aspect. ~~Future~~ For development of a robust operational method, future studies should aim to include a larger number of satellite scenes acquired ~~during~~ with various sea ice conditions, melt pond evolution stages, wind speeds, and incidence angles. The effect and limitations of sea ice surface roughness and dependency on filtering size and scale should also be further investigated.

Acknowledgements. The authors would like to thank the captain, crew and scientists from the Norwegian Polar Institute (NPI) and Airlift AS on-board R/V Lance during the expedition ICE2012 for support and data collection. The TerraSAR-X data are provided by InfoTerra. We acknowledge S. Hudson at NPI for help with meteorological data, and A. Fransson, also at NPI, for providing ice core information. Thanks to W. Dierking at the Alfred Wegner Institute and C. Brekke and T. Eltoft at Department of Physics and Technology, UiT-The Arctic University of Norway for participation in discussions, and to S. N. Anfinsen at Department of Physics and Technology, UiT-The Arctic University of Norway for useful comments on the manuscript. The project was supported financially by Regional Differensiert Arbeidsgiveravgift (RDA) Troms County, by the project "Sea Ice in the Arctic Ocean, Technology and Systems of Agreements" ("Arctic Ocean", subproject "CASPER") of the Fram ~~Center~~Centre, and by ~~Center~~ the Centre for Ice, Climate and Ecosystems at the NPI.

References

Airbus Defence and Space: Basic product specifications, 2013.

Barber, D. G., Yackel, J. J., and Hanesiak, J.: Sea Ice, RADARSAT-1 and Arctic Climate Processes: A Review and Update, Canadian Journal of Remote Sensing, 27, 51–61, 2001.

Beckers, J. F., Renner, A. H. H., Spreen, G., Gerland, S., and Haas, C.: Sea-ice surface roughness estimates from airborne laser scanner and laser altimeter observations in Fram Strait and north of Svalbard, Annals of Glaciology, 56, 235–244, doi:10.3189/2015AoG69A717, 2015.

Cloude, S. R.: The dual polarisation entropy/alpha decomposition: A PALSAR case study, in: Proc. POLinSAR 2007, 22-26 Januar 2007, European Space Agency (ESA SP-644), Frascati, Italy, 2007.

Cloude, S. R. and Pottier, E.: An entropy based classification scheme for land applications of polarimetric SAR, IEEE Transactions on Geoscience and Remote Sensing, 35, 68–78, doi:10.1109/36.551935, 1997.

Comiso, J. C. and Kwok, R.: Surface and radiative characteristics of the summer Arctic sea ice cover from multi-sensor satellite observations, Journal of Geophysical Research, 101, 28 397–28 416, doi:10.1029/96JC02816, 1996.

Corder, G. W. and Foreman, D. I.: Nonparametric Statistics for Non-Statisticians: A Step-by-step approach, John Wiley & Sons, Inc., Hoboken, USA, doi:10.1002/9781118165881, 2009.

Divine, D. V., Granskog, M. A., Hudson, S. R., Pedersen, C. A., Karlsen, T. I., Divina, S. A., Renner, A. H. H., and Gerland, S.: Regional melt-pond fraction and albedo of thin Arctic first-year drift ice in late summer, Cryosphere, 9, 255–268, doi:10.5194/tc-9-255-2015, 2015.

Divine, D. V., Pedersen, C. A., Karlsen, T. I., Aas, H. F., Granskog, M. A., Hudson, S. R., and Gerland, S.: Photogrammetric retrevals and analysis of small scale sea ice topography during summer melt, Cold Regions Science and Technology, in review, 2016.

Donelan, M. A. and Pierson, W. J.: Radar scattering and equilibrium ranges in wind-generated waves with application to scatterometry, Journal of Geophysical Research, 92, 4971–5029, doi:10.1029/JC092iC05p04971, 1987.

Doulgeris, A. P. and Eltoft, T.: Scale Mixture of Gaussian Modelling of Polarimetric SAR Data, EURASIP Journal on Advances in Signal Processing, 2010, 1–13, doi:10.1155/2010/874592, 2010.

Drinkwater, M., Kwok, R., Rignot, E., Israelsson, H., Onstott, R. G., and Winebrenner, D. P.: Potential Applications of Polarimetry to the Classification of Sea Ice, in: Microwave Remote Sensing of Sea Ice, edited by Carsey, F. D., vol. 68 of *Geophysical Monograph Series*, pp. 419–430, American Geophysical Union, Washington, DC, USA, doi:10.1029/GM068, 1992.

Ehn, J. K., Mundy, C. J., Barber, D. G., Hop, H., Rossnagel, A., and Stewart, J.: Impact of horizontal spreading on light propagation in melt pond covered seasonal sea ice in the Canadian Arctic, Journal of Geophysical Research, 116, C00G02, doi:10.1029/2010JC006908, 2011.

Eicken, H., Grenfell, T. C., Perovich, D. K., Richter-Menge, J. A., and Frey, K.: Hydraulic controls of summer Arctic pack ice albedo, Journal of Geophysical Research, 109, C08 007, doi:10.1029/2003JC001989, 2004.

Eom, H. J. and Boerner, W.-M.: Statistical properties of the phase difference between two orthogonally polarized SAR signals., Geoscience and Remote Sensing, IEEE Transactions on, 29, 182–184, 1991.

European Space Agency: Sentinel-1 toolbox - SNAP, http://step.esa.int/main/toolboxes/snap/, 2016.

Fetterer, F. and Untersteiner, N.: Observations of melt ponds on Arctic sea ice, Journal of Geophysical Research: Oceans, 103, 24 821–24 835, doi:10.1029/98JC02034, 1998.

Flocco, D., Schroeder, D., Feltham, D. L., and Hunke, E. C.: Impact of melt ponds on Arctic sea ice simulations from 1990 to 2007, Journal of Geophysical Research: Oceans, 117, doi:10.1029/2012JC008195, 2012.

Flocco, D., Feltham, D. L., Bailey, E., and Schroeder, D.: The refreezing of melt ponds on Arctic sea ice, Journal of Geophysical Research: Oceans, 120, 647–659, doi:10.1002/2014JC010140, 2015.

Fors, A. S., Doulgeris, A. P., Renner, A. H. H., Brekke, C., and Gerland, S.: On the releation between polarimetric synthetic aperture radar (SAR) features and sea ice melt pond fraction, in: Proc. IGARSS 2015, pp. 3441–3445, Milano, Italy, 2015.

Fors, A. S., Brekke, C., Doulgeris, A. P., Eltoft, T., Renner, A. H. H., and Gerland, S.: Late-summer sea ice segmentation with multi-polarisation SAR features in C and X band, The Cryosphere, 10, 401–415, doi:10.5194/tc-10-401-2016, 2016a.

Fors, A. S., Brekke, C., Gerland, S., Doulgeris, A. P., and Beckers, J. F.: Late Summer Arctic Sea Ice Surface Roughness Signatures in C-Band SAR Data, IEEE Journal of Selected Topics in Applied Earth Observations and Remote Sensing, 9, 1199–1215, doi:10.1109/JSTARS.2015.2504384, 2016b.

Hajnsek, I., Pottier, E., and Cloude, S. R.: Inversion of surface parameters from polarimetric SAR, IEEE Transactions on Geoscience and Remote Sensing, 41, 727–744, doi:10.1109/TGRS.2003.810702, 2003.

Han, H., Im, J., Kim, M., Sim, S., Kim, J., Kim, D.-J., and Kang, S.-H.: Retrieval of Melt Ponds on Arctic Multiyear Sea Ice in Summer from TerraSAR-X Dual-Polarization Data Using Machine Learning Approaches: A Case Study in the Chukchi Sea with Mid-Incidence Angle Data, Remote Sensing, 8, 57, doi:10.3390/rs8010057, 2016.

Hoaglin, D. C., Mosteller, F., and Tukey, J. W.: Understanding robust and exploratory data analysis, John Wiley & Sons, Inc, New York, 1983.

Holland, M. M., Bailey, D. A., Briegleb, B. P., Light, B., and Hunke, E.: Improved sea ice shortwave radiation physics in CCSM4: The impact of melt ponds and aerosols on Arctic sea ice, Journal of Climate, 25, 1413–1430, doi:10.1175/JCLI-D-11-00078.1, 2012.

Howell, S. E. L., Tivy, A., Yackel, J. J., and Scharien, R. K.: Application of a SeaWinds/QuikSCAT sea ice melt algorithm for assessing melt dynamics in the Canadian Arctic Archipelago, Journal of Geophysical Research: Oceans, 111, doi:10.1029/2005JC003193, 2006.

Hudson, S. R., Granskog, M. A., Sundfjord, A., Randelhoff, A., Renner, A. H. H., and Divine, D. V.: Energy budget of first-year Arctic sea ice in advanced stages of melt, Geophysical Research Letters, 40, 2679–2683, doi:10.1002/grl.50517, 2013.

Inoue, J., Curry, J. A., and Maslanik, J. A.: Application of Aerosondes to Melt-Pond Observations over Arctic Sea Ice, Journal of Atmospheric and Oceanic Technology, 25, 327–334, doi:10.1175/2007JTECHA955.1, 2008.

Istomina, L., Heygster, G., Huntemann, M., Schwarz, P., Birnbaum, G., Scharien, R., Polashenski, C., Perovich, D., Zege, E., Malinka, A., Prikhach, A., and Katsev, I.: Melt pond fraction and spectral sea ice albedo retrieval from MERIS data - Part 1: Validation against in situ, aerial, and ship cruise data, Cryosphere, 9, 1551–1566, doi:10.5194/tc-9-1551-2015, 2015.

Jeffries, M. O., Schwartz, K., and Li, S.: Arctic summer sea-ice SAR signatures, melt-season characteristics, and melt-pond fractions, Polar Record, 33, 101–112, doi:10.1017/S003224740001442X, 1997.

Kellndorfer, J., L.E., P., M.C., D., and Ulaby, F. T.: Toward consistent regional-to-global-scale vegetation characterization using orbital SAR systems, IEEE Transactions on Geoscience and Remote Sensing, 36, 1396–1411, doi:10.1109/36.718844, 1998.

Kern, S., Brath, M., and Stammer, D.: Melt Ponds as Observed with a Helicopter-Borne, Multi-Frequency Scatterometer in the Arctic Ocean in 2007, in: Proc. of ESA Living Planet Symp., European Space Agency (ESA SP-686), Bergen, Norway, 2010.

Kim, D. J., Hwang, B., Chung, K. H., Lee, S. H., Jung, H. S., and Moon, W. M.: Melt pond mapping with high-resolution SAR: The first view, Proceedings of the IEEE, 101, 748–758, 2013.

Lee, J.-S. and Pottier, E.: Polarimetric radar imaging: From basics to applications, CRC Press, Taylor and Francis Group, Boca Raton, FL, USA, 2009.

Light, B., Grenfell, T. C., and Perovich, D. K.: Transmission and absorption of solar radiation by Arctic sea ice during the melt season, Journal of Geophysical Research: Oceans, 113, doi:10.1029/2006JC003977, 2008.

Mäkynen, M., Kern, S., Rösel, A., and Pedersen, L. T.: On the Estimation of Melt Pond Fraction on the Arctic Sea Ice With ENVISAT WSM Images, IEEE Transactions on Geoscience and Remote Sensing, 52, 7366–7379, doi:10.1109/TGRS.2014.2311476, 2014.

Mardia, K. V.: Measure of multivariate skewness and kurtosis with applications, Biometrica, 57, 519—-530, 1970.

Markus, T., Cavalieri, D. J., Tschudi, M. A., and Ivanoff, A.: Comparison of aerial video and Landsat 7 data over ponded sea ice, Remote Sensing of Environment, 86, 458–469, doi:10.1016/S0034-4257(03)00124-X, 2003.

Minchew, B., Jones, C. E., and Holt, B.: Polarimetric Analysis of Backscatter From the Deepwater Horizon Oil Spill Using L-Band Synthetic Aperture Radar, IEEE Transactions on Geoscience and Remote Sensing, 50, 3812–3830, doi:10.1109/TGRS.2012.2185804, 2012.

Moen, M.-A., Doulgeris, A. P., Anfinsen, S. N., Renner, A. H. H., Hughes, N., Gerland, S., and Eltoft, T.: Comparison of feature based segmentation of full polarimetric SAR satellite sea ice images with manually drawn ice charts, The Cryosphere, 7, 1693–1705, doi:10.5194/tc-7-1693-2013, 2013.

Nicolaus, M., Katlein, C., Maslanik, J., and Hendricks, S.: Changes in Arctic sea ice result in increasing light transmittance and absorption, Geophysical Research Letters, 39, doi:10.1029/2012GL053738, 2012.

Perovich, D. K.: Aerial observations of the evolution of ice surface conditions during summer, Journal of Geophysical Research, 107, 8048, doi:10.1029/2000JC000449, 2002.

Perovich, D. K. and Polashenski, C.: Albedo evolution of seasonal Arctic sea ice, Geophysical Research Letters, 39, doi:10.1029/2012GL051432, 2012.

Perovich, D. K., Grenfell, T. C., Light, B., Elder, B. C., Harbeck, J., Polashenski, C., Tucker, W. B., and Stelmach, C.: Transpolar observations of the morphological properties of Arctic sea ice, Journal of Geophysical Research, 114, C00A04, doi:10.1029/2008JC004892, 2009.

Perovich, D. K., Meier, W. N., Tschudi, M. A., Farrell, S., Gerland, S., and Hendricks, S.: Sea ice [in Arctic Report Card 2015], http://www.arctic.noaa.gov/reportcard, 2015.

Polashenski, C., Perovich, D., and Courville, Z.: The mechanisms of sea ice melt pond formation and evolution, Journal of Geophysical Research, 117, C01 001, doi:10.1029/2011JC007231, http://doi.wiley.com/10.1029/2011JC007231, 2012.

Renner, A. H., Hendricks, S., Gerland, S., Beckers, J., Haas, C., and Krumpen, T.: Large-scale ice thickness distribution of first-year sea ice in spring and summer north of Svalbard, Annals of Glaciology, 54, 13–18, doi:10.3189/2013AoG62A146, 2013.

Rösel, A. and Kaleschke, L.: Comparison of different retrieval techniques for melt ponds on Arctic sea ice from Landsat and MODIS satellite data, Annals of Glaciology, 52, 185–191, 2011.

Rösel, A. and Kaleschke, L.: Exceptional melt pond occurrence in the years 2007 and 2011 on the Arctic sea ice revealed from MODIS satellite data, Journal of Geophysical Research: Oceans, 117, doi:10.1029/2011JC007869, 2012.

Rösel, A., Kaleschke, L., and Birnbaum, G.: Melt ponds on Arctic sea ice determined from MODIS satellite data using an artificial neural network, The Cryosphere, 6, 431–446, doi:10.5194/tc-6-431-2012, 2012.

Scharien, R. K., Yackel, J. J., Barber, D. G., Asplin, M., Gupta, M., and Isleifson, D.: Geophysical controls on C band polarimetric backscatter from melt pond covered Arctic first-year sea ice: Assessment using high-resolution scatterometry, Journal of Geophysical Research: Oceans, 117, doi:10.1029/2011JC007353, 2012.

Scharien, R. K., Hochheim, K., Landy, J., and Barber, D. G.: First-year sea ice melt pond fraction estimation from dual-polarisation C-band SAR – Part 2: Scaling in situ to Radarsat-2, The Cryosphere, 8, 2163–2176, doi:10.5194/tc-8-2163-2014, 2014a.

Scharien, R. K., Landy, J., and Barber, D. G.: First-year sea ice melt pond fraction estimation from dual-polarisation C-band SAR – Part 1: In situ observations, The Cryosphere, 8, 2147–2162, doi:10.5194/tc-8-2147-2014, 2014b.

Schröder, D., Feltham, D. L., Flocco, D., and Tsamados, M.: September Arctic sea-ice minimum predicted by spring melt-pond fraction, Nature Climate Change, 4, 353–357, doi:10.1038/nclimate2203, 2014.

Skrunes, S., Brekke, C., and Eltoft, T.: Characterization of Marine Surface Slicks by Radarsat-2 Multipolarization Features, IEEE Transactions on Geoscience and Remote Sensing, 52, 5302–5319, doi:10.1109/TGRS.2013.2287916, 2014.

Tschudi, M. A., Maslanik, J. A., and Perovich, D. K.: Derivation of melt pond coverage on Arctic sea ice using MODIS observations, Remote Sensing of Environment, 112, 2605–2614, doi:10.1016/j.rse.2007.12.009, 2008.

van Zyl, J. J. and Kim, Y.: Synthetic Aperture Radar Polarimetry, John Wiley & Sons, Inc, Hoboken, USA, 2011.

Yackel, J. J. and Barber, D. G.: Melt ponds on sea ice in the Canadian Archipelago: 2. On the use of RADARSAT-1 synthetic aperture radar for geophysical inversion, Journal of Geophysical Research, 105, 22 061, doi:10.1029/2000JC900076, 2000.

Yackel, J. J., Barber, D. G., Papakyriakou, T. N., and Breneman, C.: First-year sea ice spring melt transitions in the Canadian Arctic Archipelago from time-series synthetic aperture radar data, 1992–2002, Hydrological Processes, 21, 253–265, doi:10.1002/hyp.6240, 2007.

820 Zege, E., Malinka, A., Katsev, I., Prikhach, A., Heygster, G., Istomina, L., Birnbaum, G., and Schwarz, P.: Algorithm to retrieve the melt pond fraction and the spectral albedo of Arctic summer ice from satellite optical data, Remote Sensing of Environment, 163, 153–164, doi:10.1016/j.rse.2015.03.012, 2015.

Table 1. Overview of the satellite scenes.

Date	Time (UTC)	Scene ID	Incidence angle	Pixel spacing (az. × ground range)	Wind speed (2 m.a.s.)	Air temperature (2 m.a.s.)
28 Jul 2012	06:52	T1	36.9°	2.4 m × 1.5 m	1.6 m/s	$0.1^{\circ}C$
29 Jul 2012	14:25	T2	37.9°	2.5 m × 1.5 m	5.1 m/s	$1.1^{\circ}C$
31 Jul 2012	13:51	T3	29.4°	2.4 m × 1.9 m	6.2 m/s	$-0.8^{\circ}C$
2 Aug 2012	14:51	T4	44.2°	3.0 m × 1.3 m	0.6 m/s	$0.8^{\circ}C$

Table 2. Overview of the images captured during the helicopter flights. Only images without open water fraction are included in the study. The bottom entries show the global values derived from all five flights, and the local values of the floe investigated in T3 and T4.

Date	Time (UTC)	No. of images	Transect length	Mean f_{MP}	Std. f_{MP}
31 Jul 2012	7:36-8:10	848	67 km	30.1%	10.0%
1 Aug 2012	7:22-8:34	1364	139 km	31.1%	12.3%
1 Aug 2012	16:45-18:03	1383	154 km	34.8%	12.8%
2 Aug 2012	11:21-12:00	676	78 km	33.0%	13.7%
2 Aug 2012	14:43-16:04	1458	170 km	33.2%	11.4%
Global values	-	5729	608 km	33.2%	11.4%
Floe values	-	43	4 km	30.6%	11.1%

Table 3. Estimated sea ice surface roughness (s_{RMS}) from five segments at the floe by R/V Lance. Values in parenthesis displays standard deviations (std) of s_{RMS}.

Segment Nr.	Area	s_{RMS} $(std(s_{RMS}))$
1	11000 m^2	6.7 (0.3) cm
2	13530 m^2	11.0 (10) cm
3	11670 m^2	7.4 (0.6) cm
4	13820 m^2	9.0 (0.4) cm
5	12380 m^2	10.0 (0.4) cm

Table 4. Spearman's correlation coefficient (r) between f_{MP} retrieved from the helicopter images at the investigated floe, and mean and standard deviation of the polarimetric SAR features from the corresponding area in T3 and T4. Bold indicate significant values within a 95% confidence interval, and values in parentheses are ~~retrived after including~~ retrieved before NESZ subtraction in the calibration process.

	r (T3)		r (T4)	
SAR feature	Mean	Std.	Mean	Std.
σ^0_{HH}	~~0.05 (~~0.04 (0.05)	~~0.09 (~~0.10 (0.09)	~~**-0.32**~~**-0.33** (**-0.33**)	~~-0.22 (~~-0.27 (-0.22)
σ^0_{VV}	0.21 (0.21)	0.09 (0.09)	~~**-0.53** (~~**-0.54** (**-0.53**)	~~**-0.52** (~~**-0.54** (**-0.52**)
$R_{VV/HH}$	~~**0.46** (~~**0.45** (**0.46**)	~~-0.07 (~~0.03 (-0.07)	**-0.31** (**-0.31**)	~~-0.01 (~~**-0.48** (-0.01)
H	~~0.21 (~~0.11 (0.21)	~~0.14 (~~0.25 (0.14)	~~**0.45** (~~0.22 (**0.45**)	~~0.07 (~~-0.17 (0.07)
α_1	~~0.26 (~~**0.40** (0.26)	~~0.17 (~~0.00 (0.17)	~~-0.18 (~~-0.24 (-0.18)	~~0.30 (~~0.11 (0.30)
RK	~~0.03 (~~0.07 (0.03)	~~0.04 (~~0.07 (0.04)	~~0.04 (~~-0.15 (0.04)	~~0.13 (~~0.08 (0.13)
$\lvert\rho\rvert$	~~-0.22 (~~-0.13 (-0.22)	~~-0.00 (~~0.04 (0.00)	~~**-0.40** (~~-0.17 ~~) -0.06 ((~~~~**-0.44**~~**-0.40**)	**-0.44**(-0.06)
$\angle\rho$	~~0.01 (~~-0.14 (0.01)	~~0.23 (~~0.10 (0.23)	~~-0.10 (~~-0.08 (-0.10)	~~**0.55** (~~0.12(**0.55**)

Table 5. Statistics of modeled f_{MP} distributions.

		$f_{MP}(R_{VV/HH})$		$f_{MP}(\sigma^0_{VV})$	
Area	Window size (pixels)	Mean	Std.	Mean	Std.
T3, floe	21×21	34.9%	~~25.14%~~ 24.8%	-	-
T3, floe	51×51	35.0%	~~11.1%~~ 11.0%	-	-
T4, floe	21×21	-	-	~~32.4%~~30.6%	~~23.6%~~ 26.0%
T4, floe	51×51	-	-	~~31.9%~~ 31.4%	~~15.0%~~ 16.7%
T1, full scene	51×51	~~36.2%~~36.5%	~~12.6%~~12.3%	~~−6.1%~~19.0%	~~23.9%~~29.9%
T2, full scene	51×51	~~45.7%~~45.1%	~~13.6%~~13.3%	~~−19.5%~~−1.6%	~~19.0%~~27.8%
T3, full scene	51×51	31.2%	~~11.3%~~11.2%	~~−32.6%~~19.7%	~~23.3%~~29.7%
T4, full scene	51×51	~~53.3%~~51.9%	~~13.5%~~12.3%	~~28.2%~~36.3%	~~14.0%~~15.7%

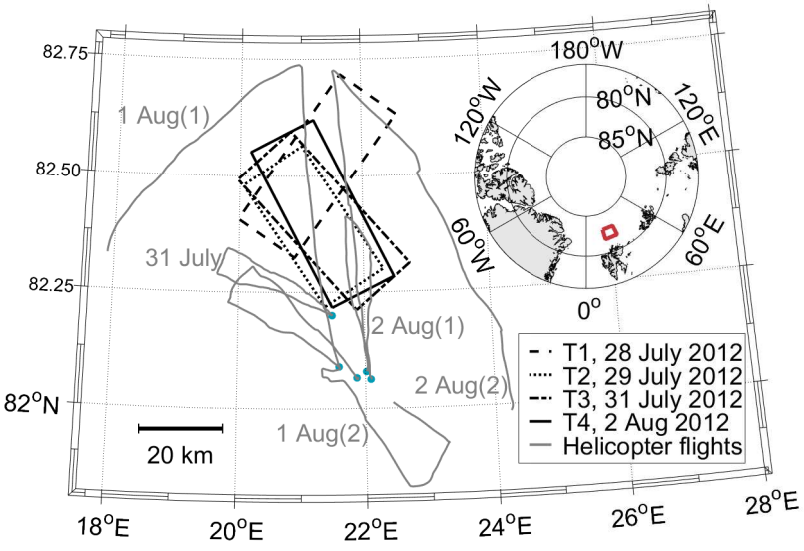

Figure 1. Map of the study area north of Svalbard, showing the location of the satellite scenes and the track of the helicopter flights. Blue dots mark the starting points of the flights. The red box in the inset map of the northern hemisphere shows the geographical position of the area displayed.

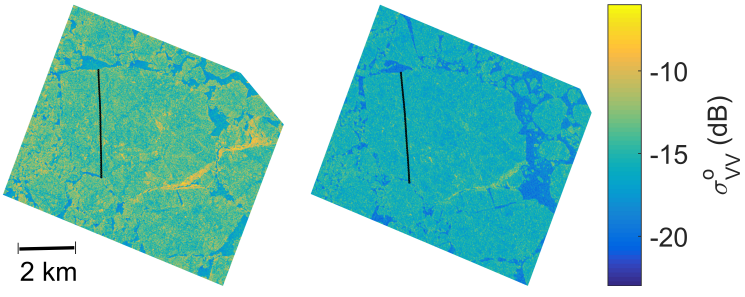

Figure 2. The floe investigated in scene T3 (left) and T4 (right). The black line marks the transect along which the helicopter image were taken.

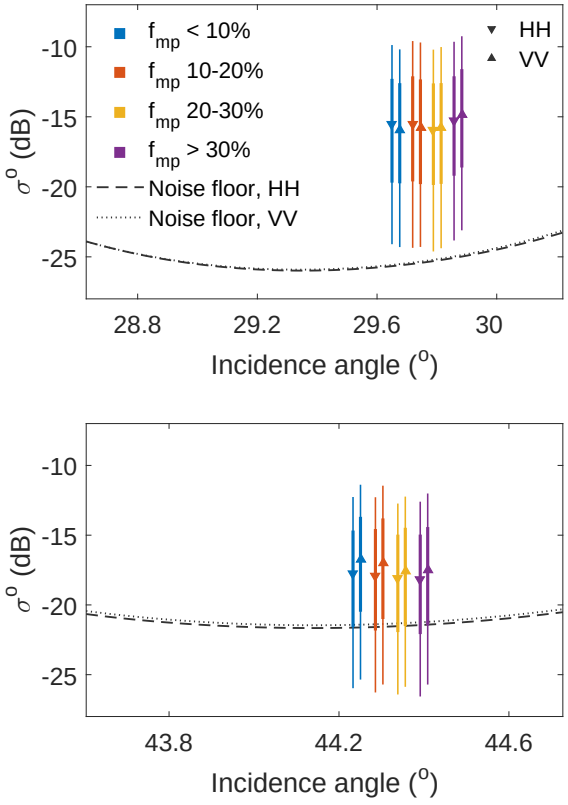

Figure 3. Signal-to-noise analysis of HH and VV channels for areas with different f_{mp} retrieved from the investigated floe in scene T3 (top) and T4 (bottom). The triangles displays the median of σ^0_{HH} (dB) (upward pointing) and σ^0_{VV} (downward pointing). The thin line represents the part of σ^0 falling between the 10 and the 90 percentile, while the thick line represents the part of σ^0 falling between the 25 and 75 percentile. Hence, the lines indicate the distributions. All markers are offset from the middle position for clarity.

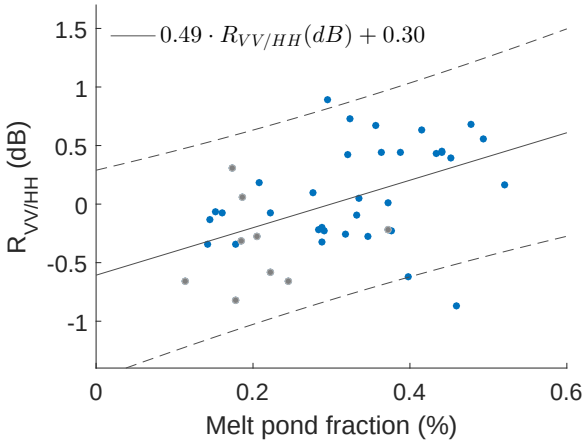

Figure 4. Scatter plot displaying f_{MP} retrieved from the 43 helicopter images covering the investigated floe in T3, and mean $R_{VV/HH}$ extracted from the corresponding areas. Grey dots represent areas with partly deformed sea ice, wile blue dots represent areas of level ice. The trend line represents a robust bisquare weights least squares linear fit of the data, and the dotted line represent the 95% confidence interval of the regression. R^2_{fit} equals 0.21.

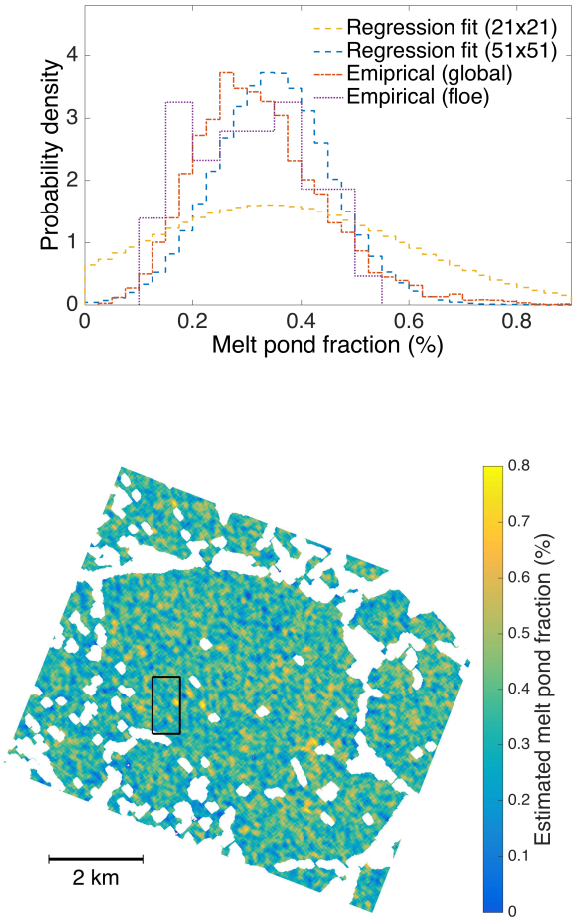

Figure 5. Top: Probability density distributions of f_{MP} for the investigated floe in T3. Curves represent distributions produced by the ~~model~~ regression fit based on $R_{VV/HH}$ with 21×21 and 51×51 pixels windows, and empirical distributions from all helicopter flights (global) and from the specific floe (floe). Bottom: Estimated f_{MP} from the $R_{VV/HH}$ based ~~model~~ regression with a 51×51 pixels window for investigated floe in T3. The frame outlines the area displayed in Fig. 6.

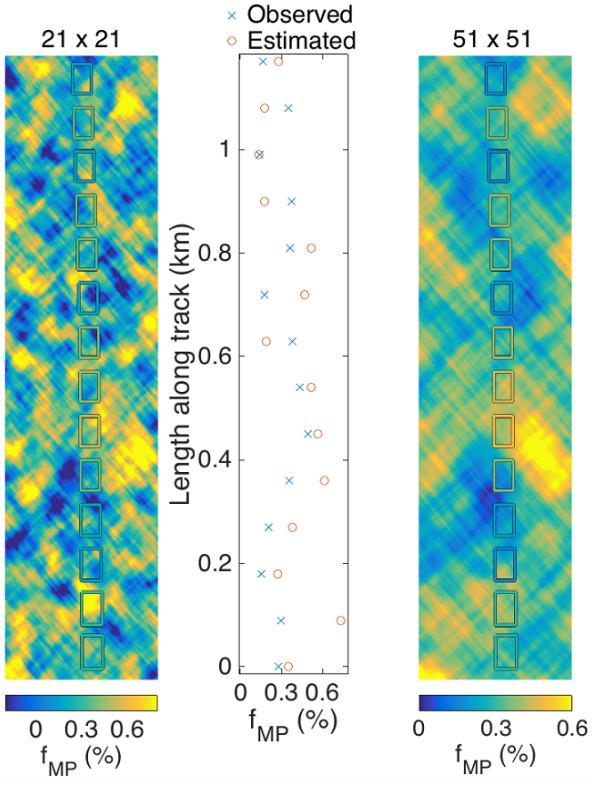

Figure 6. Melt pond fraction (f_{MP}) estimated from $R_{VV/HH}$, with the observed f_{MP} from the helicopter images overlaid as colored frames. The area displayed is outlined with a frame in Fig. 5. The estimation is performed with 21×21 (left) and 51×51 (right) pixels windows. Note that the center pixel underlying each helicopter image frame would give the most representative value for comparison to the observed f_{MP}, as pixels closer to the frame contain a larger amount of information from outside the frame. The middle panel displays the mean estimated f_{MP} value for each frame together with the observed value.

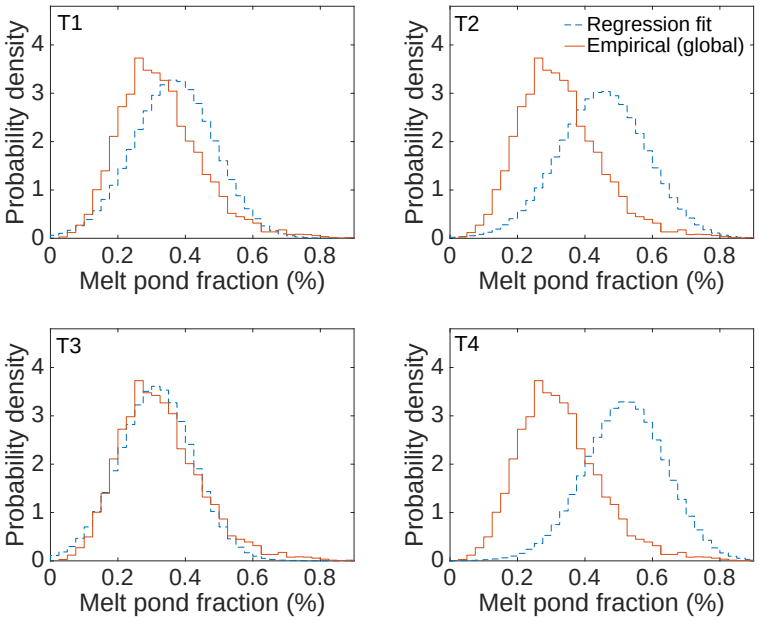

Figure 7. Probability density distributions of f_{MP} for the four investigated scenes (T1-T4). Curves represent distributions produced from the $R_{VV/HH}$ based ~~model~~ regression fit with a 51×51 pixels window, and the empirical distribution retrieved from all five helicopter flights.

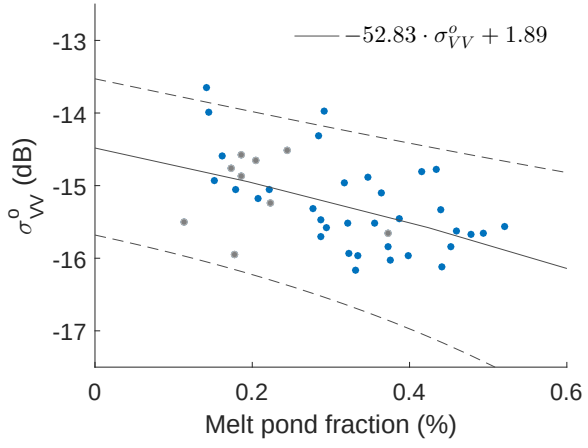

Figure 8. Scatter plot displaying f_{MP} retrieved from the 43 helicopter images covering the investigated floe in T4, and mean σ^0_{VV} extracted from the corresponding areas. Grey dots represent areas with partly deformed sea ice, while blue dots represent areas of level ice. The trend line represents a robust bisquare weights least squares linear fit of the data, and the dotted line represent the 95% confidence interval of the regression. R^2_{fit} equals 0.26.

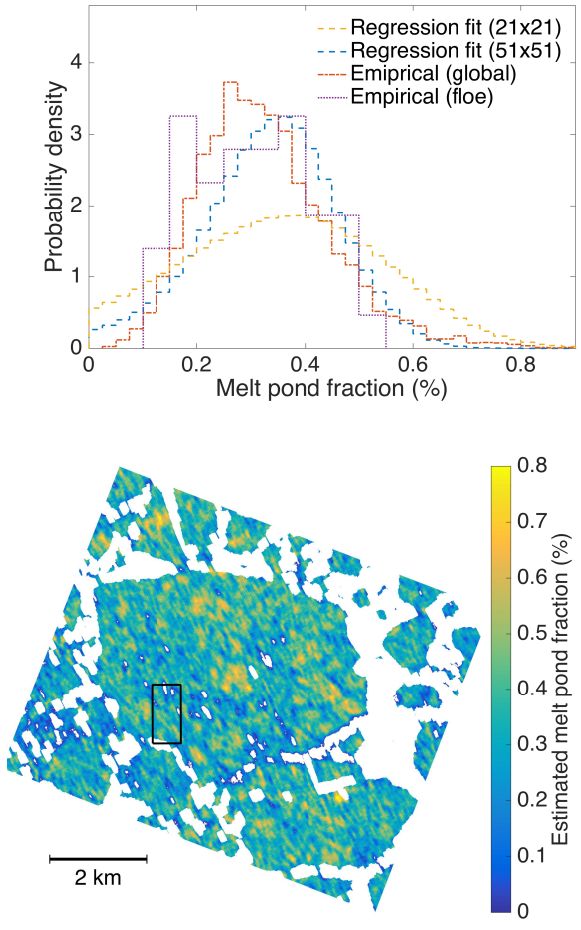

Figure 9. Top: Probability density distributions of f_{MP} for the investigated floe in T4. Curves represent distributions produced by the ~~model~~ regression fit based on σ^0_{VV} with 21×21 and 51×51 pixels windows, and empirical distributions from all helicopter flights (global) and from the specific floe (floe). Bottom: Estimated f_{MP} from the σ^0_{VV} based ~~model~~ regression with a 51×51 pixels window for investigated floe in T4. The frame outlines the area displayed in Fig. 10.

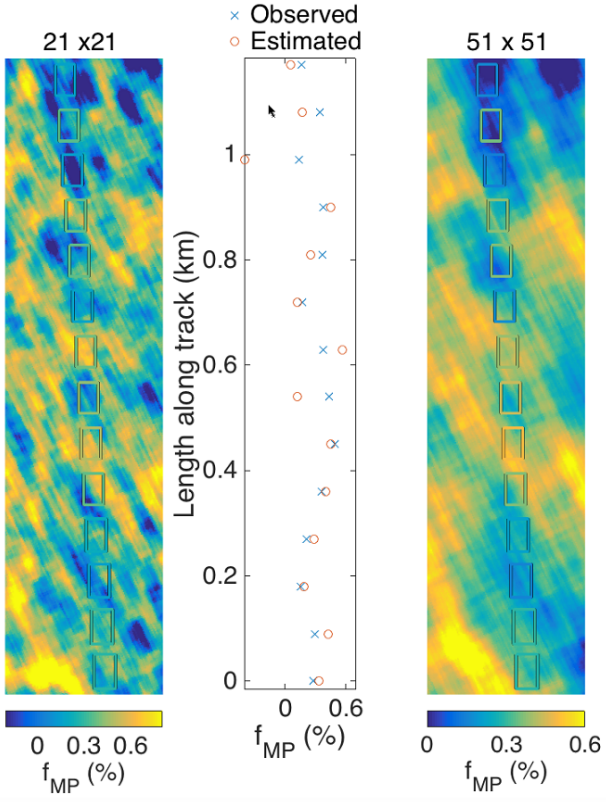

Figure 10. Melt pond fraction (f_{MP}) estimated from $sigma^0_{VV}$, with the observed f_{MP} from the helicopter images overlaid as colored frames. The area displayed is outlined with a frame in Fig. 9. The estimation is performed with 21×21 (left) and 51×51 (right) pixels windows. Note that the center pixel underlying each helicopter image frame would give the most representative value for comparison to the observed f_{MP}, as pixels closer to the frame contain a larger amount of information from outside the frame. The middle panel displays the mean estimated f_{MP} value for each frame together with the observed value.

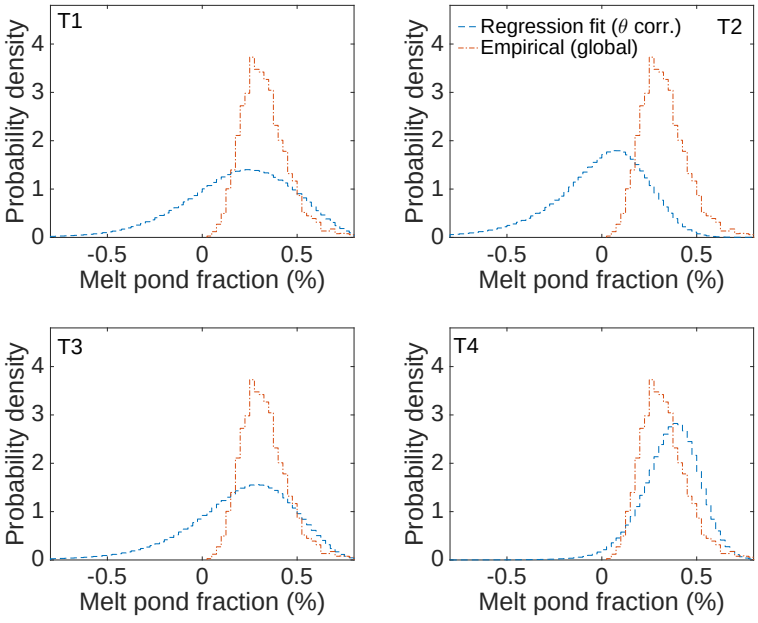

Figure 11. Probability density distributions of f_{MP} for the four investigated scenes (T1-T4). Curves represent distributions produced from the σ^0_{VV} based ~~model~~ regression with a 51×51 pixels window, and the empirical distribution retrieved from all five helicopter flights.